Journal of Materials Chemistry C

ROYAL SOCIETY OF CHEMISTRY

REVIEW

View Article Online
View Journal | View Issue

Cite this: J. Mater. Chem. C, 2025, 13, 9930

Received 13th January 2025,
Accepted 15th March 2025

DOI: 10.1039/d5tc00145e

rsc.li/materials-c

Bimetal-decorated resistive gas sensors: a review

Ka Yoon Shin,[a] Yujin Kim,[b] Ali Mirzaei,*[c] Hyoun Woo Kim*[a] and Sang Sub Kim *[b]

Various noble metals such as Au, Ag, Pd, Pt, Ru, and Rh are used for decorating resistive gas sensors because of their high catalytic activity and electronic effects, which boost the overall sensing characteristics of resistive sensors. However, bimetallic decorations such as AuPt, AuPd, PtPd, and AuAg are often preferred to boost the sensing capabilities because bimetallic combinations exert synergistic effects that enhance the catalytic features compared with that of their single-metal-decorated counterparts. In this review, we discuss the roles of different bimetallic couples in the sensing capacity of resistive sensors with specific emphasis on the underlying sensing mechanism. We believe that this review will be highly beneficial for researchers working in the field of gas sensors.

1. Introduction

The rapid development and progress achieved in various industries and the automobile sector coupled with population increase have resulted in air pollution becoming a major issue in most countries. Particulate matter (PM), NO_2, SO_2, O_3, and CO are the major contributors to air pollution.[1,2] Additionally, volatile organic compounds (VOCs) such as toluene (C_7H_8), acetone (C_3H_6O), formaldehyde (HCHO), and trimethylamine (C_3H_9N; TMA) that exhibit low boiling points (50–260 °C), high vapor pressure (133.3 Pa), and high volatility contribute to air pollution, particularly to indoor air pollution.[3] VOCs are classified into several categories based on their boiling points, molecular structures, and polarities (Fig. 1).[4] Exposure to VOCs causes respiratory irritation and asthma.[5] Furthermore, exposure to aromatic VOCs causes cancer, obesity, diabetes, and damage to the nervous system.[6]

Additionally, other gases such as H_2S, H_2, and CH_4 that are present in air are toxic or explosive. For example, CH_4 is common in coal mines,[7] and H_2S is common in the oil and gas industry.[8] From an environmental perspective, the major effects of toxic gases include acid rain, ozone layer depletion, ozone-forming photochemical reactions, and global warming.[9,10] From a human health perspective, exposure to polluted air accounts for one-quarter of the morbidity/mortality associated with heart disease and one-quarter of stroke cases.[11] Fig. 2 presents three primary hypotheses that relate cardiovascular impairment with air pollution.[12]

In addition to their toxic effects, some gases and VOCs act as biomarkers that enable the diagnosis of certain diseases such as asthma, lung cancer, oxidative stress, metabolic illness, and diabetes

[a] Division of Materials Science and Engineering, Hanyang University, Seoul 04763, Republic of Korea. E-mail: hyounwoo@hanyang.ac.kr
[b] Department of Materials Science and Engineering, Inha University, Incheon 22212, Republic of Korea. E-mail: sangsub@inha.ac.kr
[c] Department of Materials Science and Engineering, Shiraz University of Technology, Shiraz 715557-13876, Islamic Republic of Iran. E-mail: mirzaei@sutech.ac.ir

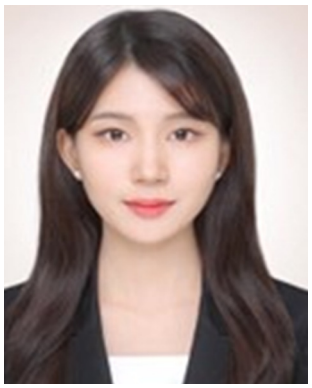

Ka Yoon Shin

Ka Yoon Shin received her BS degree in Materials Science and Engineering from Inha University in 2020 and MS degree from Hanyang University. She is currently a PhD candidate at Hanyang University. Her research interests include metal oxide gas sensors and nanostructure synthesis.

Yujin Kim

Yujin Kim graduated from the Department of Materials Science and Engineering, Kongju National University, Republic of Korea in 2023. She is now pursuing her MS degree at Inha University, Republic of Korea. She has been working on 2-dimensional transition metal dichalcogenides and 3-dimensional oxide materials for gas sensors such as MOFs.

based on their presence in the exhaled breath of patients.[13,14] Table 1 presents the characteristics of toxic gases and VOCs.

For these reasons, the detection of various gases and VOCs using reliable and robust devices is important from safety and medical perspectives. Traditionally, gas chromatography–mass spectrometry (GC–MS), selected ion flow tube mass spectrometry (SIFT-MS), and proton transfer reaction mass spectrometry (PTR-MS) have been used to detect VOCs.[19] However, these are expensive and time consuming techniques that require bulky equipment and skilled operators; hence, their applications are limited in this area.[20] Therefore, small, portable, and highly sensitive electronic devices are used as gas sensors to detect gases and VOCs.

Ali Mirzaei

Ali Mirzaei received his PhD degree in Materials Science and Engineering from Shiraz University in 2016. He was a visiting student at Messina University, Italy, in 2015 and from 2016 to 2018, he was accepted as a postdoctoral fellow at Hanyang University, Korea. Also, in 2022 he was accepted as a researcher in Hanyang University through the Brain Pool program. He is the author or co-author of 225 peer-reviewed papers, including 30 review papers. Currently, he is the assistant professor of materials science and engineering at the Shiraz University of Technology, Iran. He is interested in the synthesis and characterization of nanocomposites for gas sensing applications.

2. Resistive gas sensors

Resistive sensors are most popular among the different gas sensors because of their high sensitivity, fast dynamics, simple design, low price, and high stability.[21] The first resistive gas sensor was introduced in 1962 in Japan by Seiyama *et al.*[22] Since then, extensive research has been conducted to develop highly sensitive and reliable sensors.[23] Two design strategies are primarily used for fabricating gas sensors. The planar design strategy uses a flat substrate of insulating nature, which is equipped with interdigitated electrodes and a heater attached to the backside. Then, the sensing material is deposited on the front side of the sensor to make it ready for use (Fig. 3(a)). Tubular gas sensors use a small insulating tube, such as alumina, as the substrate equipped with electrodes and a resistive Ni–Cr wire to heat the sensor to the desired temperature. The sensing material is deposited over the substrate to make the gas sensor ready for use (Fig. 3(b)).[24]

Resistive gas sensors are composed primarily of semiconducting metal oxides owing to their widespread availability, stability, semiconducting nature, cost-effectiveness, ease of synthesis, and excellent electrical properties.[25] When a resistive gas sensor is exposed to air, oxygen molecules will be adsorbed on its surface and thanks to the high electron affinity of oxygen, it takes electrons from the sensor surface by the following reactions:[26]

$$O_2^-(ads) + e^- \rightarrow 2O^-(ads) \quad (1)$$

$$O_2(ads) + e^- \rightarrow O_2^-(ads) \quad (2)$$

$$O_2^-(ads)e^- \rightarrow 2O^-(ads) \quad (3)$$

$$O^-(ads) + e^- \rightarrow O^{2-}(ads) \quad (4)$$

Hyoun Woo Kim

Hyoun Woo Kim joined the Division of Materials Science and Engineering at Hanyang University as a full professor in 2011. He received his BS and MS degrees from Seoul National University and his PhD degree from the Massachusetts Institute of Technology (MIT) in Electronic Materials in 1986, 1988, and 1994, respectively. He was a senior researcher at Samsung Electronics Co. Ltd. from 1994 to 2000. He was a professor of materials science and engineering at Inha University from 2000 to 2010. He was a visiting professor at the Department of Chemistry of the Michigan State University, in 2009. His research interests include one-dimensional nanostructures, nanosheets, and gas sensors.

Sang Sub Kim

Sang Sub Kim joined the Department of Materials Science and Engineering, Inha University in 2007 as a full professor. He received his BS degree from Seoul National University and his MS and PhD degrees from the Pohang University of Science and Technology (POSTECH) in Materials Science and Engineering in 1987, 1990, and 1994, respectively. He was a visiting researcher at the National Research in Inorganic Materials (currently NIMS), Japan for 2 years each in 1995 and in 2000. In 2006, he was a visiting professor at the Department of Chemistry, University of Alberta, Canada. In 2010, he also served as a cooperative professor at the Nagaoka University of Technology, Japan. His research interests include the synthesis and applications of nanomaterials such as nanowires and nanofibers, functional thin films, and surface and interfacial characterization methods.

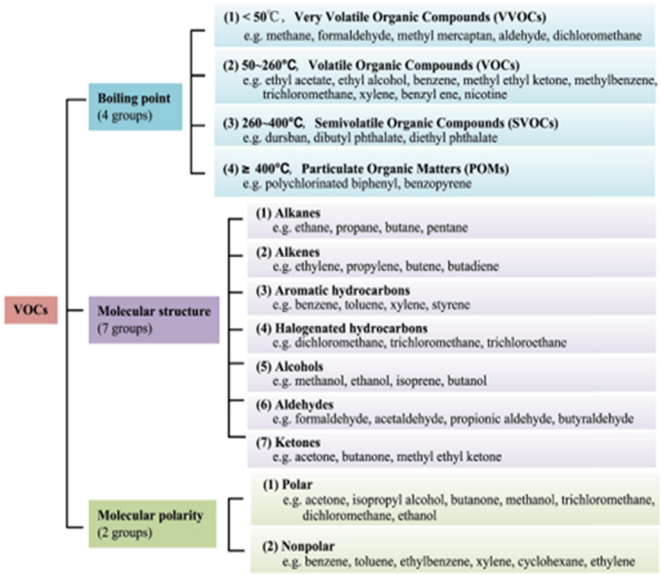

Fig. 1 VOC classification. Reproduced with permission from MDPI, ref. 4.

For n-type gas sensors, the above reactions cause the depletion of the outer layer of sensing materials and the so-called electron depletion layer (EDL) will be formed in air. Since the concentrations of electrons in this layer are much lower than those in inner parts of the sensing layer, overall, the resistance of the sensor increases, relative to vacuum conditions. For p-type gas sensors, capture of electrons by adsorbed oxygen species causes the formation of a hole accumulation layer (HAL), in which the concentration of holes is higher than those in inner parts, and the resistance of the sensor decreases relative to vacuum. Upon exposure to a reducing gas, the gas reacts with the already adsorbed oxygen species, causing the release of the electrons on the sensing layer, and as a result, the thickness of the EDL and the HAL for n- and p-type gas sensors decreases, respectively. This modulation of the thickness of layers eventually causes the modulation of resistance, where the resistance of n-type gas sensors decreases, while that of p-type gas sensors increases in the presence of a reducing gas. Also, upon exposure to oxidizing gases, more electrons are abstracted from the sensor surface, causing expansion of the thickness of the EDL and the HAL for n- and p-type gas sensors, respectively. This causes the increase of resistance of n-type gas sensors while for p-type sensors a decrease of the resistance occurs.[27] Fig. 4 schematically shows the general sensing mechanism of n-type and p-type gas sensors. However, they present two major issues of high working temperature and relatively weak selectivity.[28] Elevated sensing temperatures lead to high power consumption, which limits their applications in remote areas where power shortage may be common. Weak selectivity

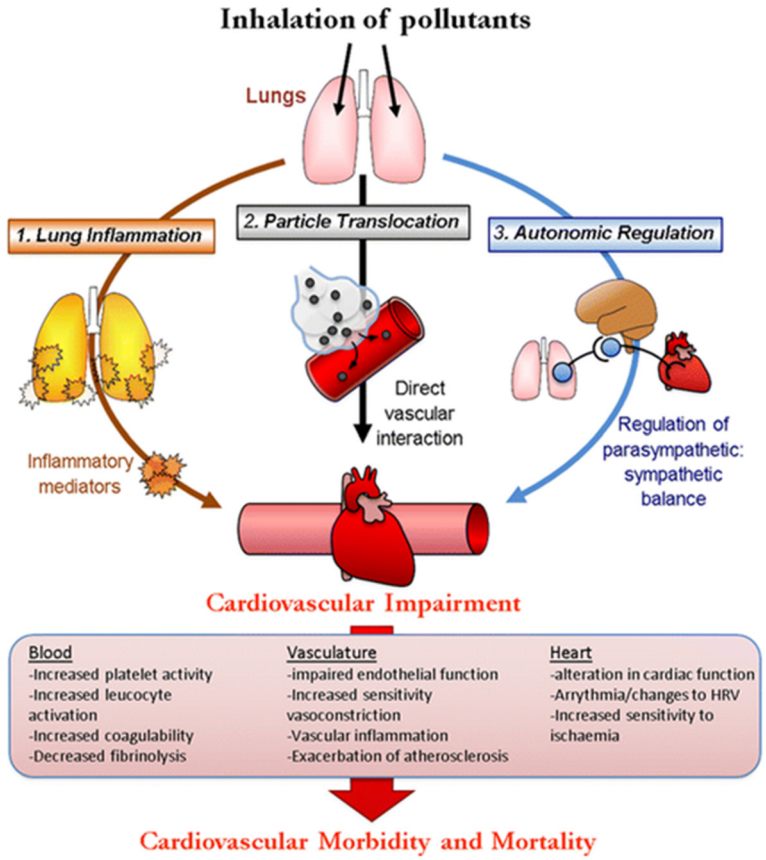

Fig. 2 Three primary hypotheses expounding on inhaled particle-mediated cardiovascular impairment. Reproduced with permission from Springer Nature, ref. 12.

Table 1 Characteristics of toxic gases and volatile organic compounds (VOCs)[15–18]

				Effects on humans and environment	
Name	Formula	Properties	Sources	Moderate	Severe
Nitrogen dioxide	NO_2	Pungent smell and reddish color	Fossil fuel industry, automotive emissions, household fuel-based appliances	Nose and throat discomfort, transient coughs, eye irritation, fatigue, and nausea	Generating ozone and acid rain, bronchitis, pulmonary edema, and asthma
Sulfur dioxide	SO_2	Colorless and pungent odor	Oxidation of sulfur-containing minerals during heating and combustion, particularly when coal is used as dominant fuel	Nose and throat discomfort, transient coughs, eye irritation, fatigue, and nausea	Respiratory and cardiovascular diseases, congestive heart failure, asthma, acute bronchitis and altered lung function, acid rain, photochemical smog, tropospheric ozone, and regional haze
Carbon monoxide	CO	Colorless, odorless, and tasteless	Fossil fuel burning	Headache, dizziness, and nausea	Death
Hydrogen sulfide	H_2S	Colorless, poisonous, malodorous, and flammable	Oil and gas industries, coke burning, paper manufacturing	Headache, dizziness, nausea, loss of memory, and olfactory paralysis	Halitosis, Down's syndrome, Alzheimer's disease, and death
Acetone	C_3H_6O	Colorless, pungent odor, flammable, and explosive	Rubber, leather, fiber, and paint	Irritation to eyes, throat, and nose	Dizziness, nausea, headache, and negative impact on the nervous system
Ethanol	C_2H_5OH	Colorless, sweetish taste and smell, low toxicity, and flammable	Acetic acid, dyes, fuels, beverages, flavors, and medical disinfectants	Headache and irritation to the mucous membrane, eyes, and nose	Dizziness, nausea, and drowsiness
Trimethylamine	C_3H_9N	Toxic, flammable, and strong odor	Solvent, antiseptic, curing agent, and synthetic dye	Irritation to the respiratory tract and damage to the mucosa and skin	Headache, pulmonary edema, and skin burn
Formaldehyde	HCHO	Toxic flammable, pungent odor, and colorless	Home furnishings and building materials	Irritation to skin, eyes, throat, and nose, nausea, coughing, and sick building syndrome	Chronic toxicity, pulmonary damage, nasopharyngeal cancer, and probably leukemia
Toluene	C_7H_8	Flammable, slightly acute toxicity, aromatic odor, and colorless	Diluents, interior decoration adhesives, and automotive interior parts	Irritation to the respiratory tract	Confusion, vomiting, convulsions, and coma
Methane	CH_4	Colorless, odorless, tasteless, and explosive	Coal mine and natural gas reservoirs	Coughing and irritation to throat, eyes, and nose	Climate change, global warming, suffocation, and death

may lead to false alarms, which causes problems in practical applications. To mitigate these shortcomings, various strategies such as heterojunction formation,[29] doping,[30] irradiation with high-energy beams,[31] morphology engineering,[32] and decoration with metals[33] have been used.

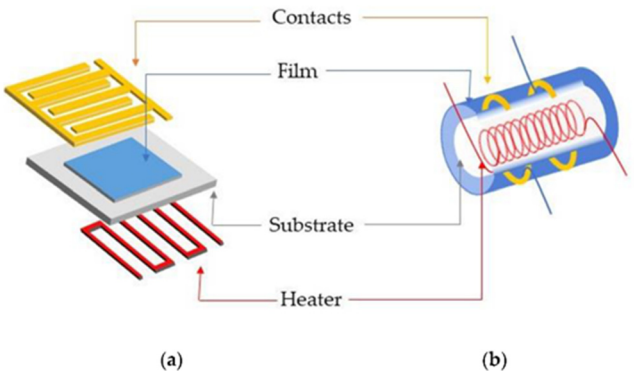

Fig. 3 (a) Flat and (b) tubular gas sensors. Reproduced with permission from MDPI, ref. 24.

Among these, noble metal decoration is a notable strategy owing to the catalytic and electronic effects of noble metals. Generally, noble metals exhibit high catalytic activity towards oxygen and some other gases. Therefore, oxygen molecules will preferentially adsorb on the surface of noble metal NPs and readily dissociate into atomic species under low activation energies. Then, the dissociated oxygen atoms move towards the metal oxides through a spill over effect. This leads to the

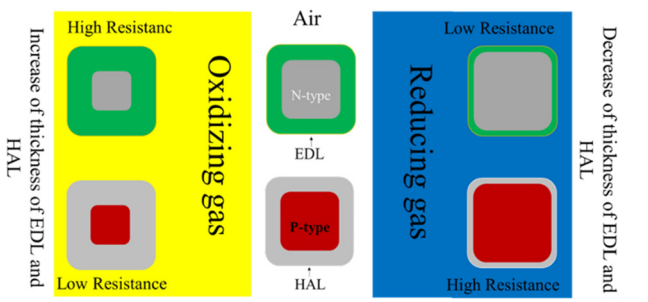

Fig. 4 General gas sensing mechanism of n- and p-type resistive gas sensors in the presence of oxidizing and reducing gases.

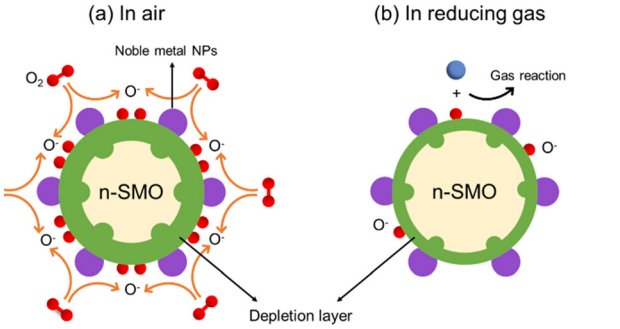

Fig. 5 Catalytic effect of noble metals for enhanced gas response of resistive gas sensors.

adsorption of more oxygen species, which in turn may mediate more reactions with the target gases and enhance the sensing signal.[34] This mechanism is schematically shown in Fig. 5(a) and (b) for an n-type gas sensor. Electronic sensitization of noble metals also significantly affects the resistance modulation. Generally, noble metals have a higher work function relative to metal oxides. Hence, in the interfaces between decorated noble metal NPs and metal oxides, the electrons move from metal oxides to noble metals to equate the Fermi levels in both sides of the interface. For n-type gas sensors this causes the formation of Schottky barriers in interfaces and also expands the thickness of the EDL. Hence, the resistance of the sensor in the presence of noble metals is higher relative to pristine form. When the sensor is exposed to a reducing gas, the released electrons cause a significant decrease of the height of Schottky barriers and also narrowing of the EDL, resulting in a remarkable change in resistance. This mechanism is schematically shown in Fig. 6(a)–(c) for n-type gas sensors. This provides a higher resistance modulation compared with that provided by the unmodified sensors.[35,36]

A bimetallic decoration strategy has been proposed to enhance the effect of metal decoration.[37] Owing to their synergistic effects, bimetallic nanoparticles (NPs) exhibit a better sensitivity than single-metal-decorated NPs. In the following sections, we present the effects of bimetal-decorated NPs on the gas-sensing behaviour of resistive sensors.

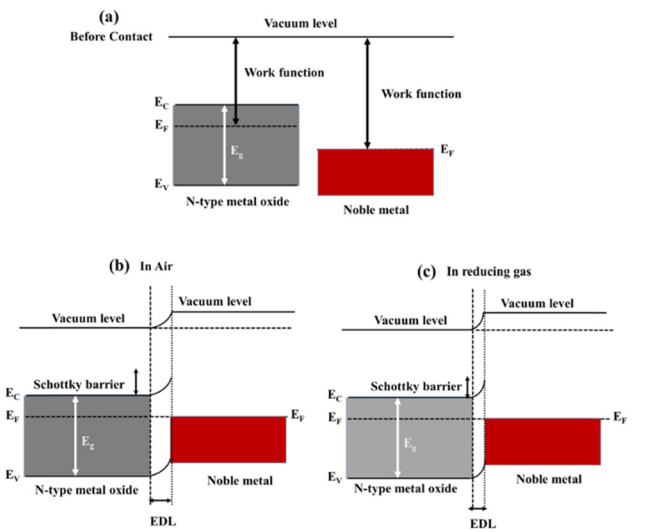

Fig. 6 Energy band levels of noble metals and n-type metal oxides before contact (a) and energy band levels after contact in (b) air and (c) reducing gas atmospheres.

3. Bimetal-decorated resistive gas sensors

Bimetallic NPs exhibit high catalytic activity and good stability, and they may increase the surface area of the sensing layer.[38–40] They exhibit better catalytic effects and selectivity than individual noble metals because of their synergistic electronic and structural interactions.[41] In addition to the enhanced sensitivity, bimetallic decoration may increase the stability of resistive gas sensors relative to its single metal-decorated counterpart. For example, alloying Au with Ag led to enhanced thermal stability of Ag, which was beneficial for gas sensing performance.[42] Also, poor stability of Pd caused by volume changes and its oxidation in an air atmosphere can be addressed by use of AuPd bimetallic decoration.[43] Thus, bimetallic NPs exert promising effects on gas sensing output.[42,44–49] In this section we will explain some notable research studies in the field of bimetal decorated gas sensors.

Alwan *et al.*[50] decorated porous silicon (P-Si) with Au, Pd, and AuPd bimetallic NPs. P-Si was fabricated through photoelectrochemical etching, followed by immersion in an Au and Pd salt solution for different immersion periods to synthesize the Au, Pd, and AuPd NP/P-Si samples (Fig. 7). Fig. 8(a) shows the SEM image of the Au NPs deposited on P-Si. Square-shaped pores were formed, and the Au NPs were spread evenly over these pores. The Au NP sizes varied from 75 to 475 nm, and the most prominent peak was observed at 75 nm (Fig. 8(d)). Also, Fig. 8(b) shows the SEM image of the Pd NPs deposited on P-Si. The sizes ranged from 75 to 375 nm, and the most significant peak was observed at 75 nm (Fig. 8(e)). Fig. 8(c) presents the SEM image of the Au–Pd bimetallic NPs, which were clustered around the surface pores rather than within them. Their sizes were approximately 30–190 nm, which were smaller than those of the monometallic nanoparticles (Fig. 8(f)).

Among the fabricated gas sensors, the AuPd bimetal-decorated sensor exhibited the highest sensitivity to CO gas. The improved gas response was attributed to the higher barrier height of the AuPd bimetal-decorated sensor than those of other gas sensors. This induced a notable change in the barrier height in the CO atmosphere, leading to the generation of a noticeable sensor signal. Furthermore, the smaller size of the bimetallic NPs than those of single NPs provided a higher surface area than those of single-metal-decorated sensors. This increased the number of surface sites for incoming gas molecules. A related study conducted by the same team showed that P–Si decorated with Au–Ag bimetallic NPs exhibited enhanced CO_2 sensing features.[51]

Pd forms PdH_x in the presence of H_2 gas by expanding substantially up to 600 times its original volume.[52] This property makes Pd a suitable material for H_2 gas sensing, which is achieved through two primary methods. The first approach

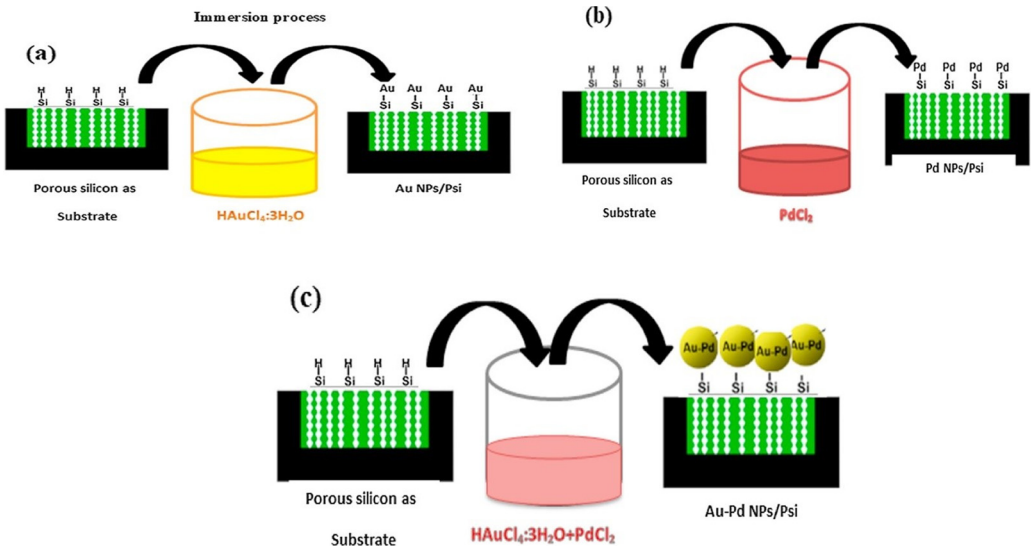

Fig. 7 Synthesis of (a) Au-, (b) Pd-, and (c) AuPd-decorated P–Si. Reproduced with permission from Elsevier, ref. 50.

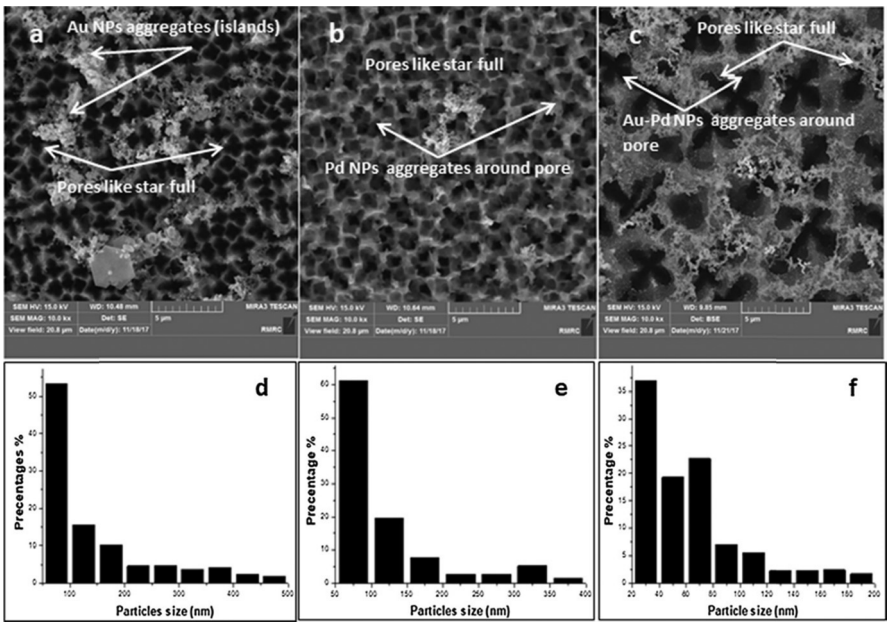

Fig. 8 Scanning electron microscopy (SEM) images and particle size distribution of (a) and (d) Au-, (b) and (e) Pd-, and (c) and (f) Au–Pd NPs. Reproduced with permission from Elsevier, ref. 50.

involves detecting changes in electrical resistance during the absorption of H_2 gas by a Pd thin film at RT.[53,54] The second approach used Pd as a catalyst to facilitate the decomposition of H_2 molecules on the surface of resistive gas sensors.[55–57] However, this catalyst is prone to oxidation into PdO at high temperatures, which reduces its H_2 adsorption capacity. Ultimately, this leads to a decline in the sensing performance. In this context, Kim *et al.*[58] synthesized bimetallic $Au_{65}Pd_{35}$ alloy NPs and mixed them (100, 300, 500, 700, and 1000 μL) with 40 mg of SnO_2 powder to enhance the H_2 sensing performance. The average size of the $Pd_{35}Au_{65}$ alloy NPs was 15 nm and that of SnO_2 NPs was 50–300 nm. The XPS study showed that the sample prepared using 500 μL of $Au_{65}Pd_{35}$ alloy NPs showed the highest percentage of adsorbed oxygen species, which are required for oxidizing H_2 gas. Additionally, the sensor fabricated from this sample showed the highest response of 72.78 to 100 ppm H_2 at 150 °C. Furthermore, the responses to H_2 gas were 7.18, 18.15, 21, and 58 times higher than those to C_2H_5OH, C_3H_6O, CO, and CH_4, respectively. Sensors with higher quantities of Pd–Au NPs exhibited reduced responses owing to agglomeration and screening effects caused by the AuPd alloy. The underlying sensing mechanism is attributed to

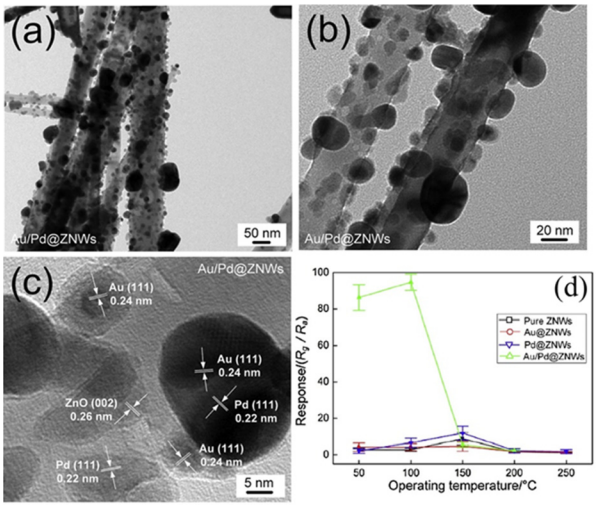

Fig. 9 (a) and (b) TEM and (c) HRTEM images of AuPd–ZnO NWs and (d) response of gas sensors to 1 ppm NO_2 *versus* temperature. Reproduced with permission from Elsevier, ref. 60.

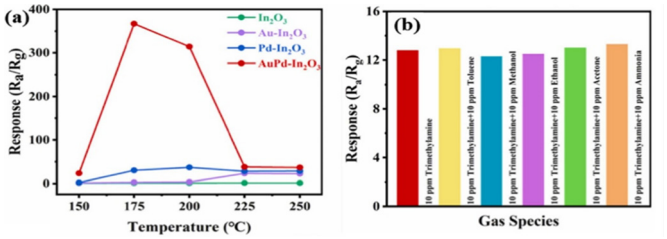

Fig. 10 (a) Gas sensing response of various gas sensors to 100 ppm C_3H_9N; (b) selectivity of the AuPd–In_2O_3 sensor to 10 ppm gas and 10 ppm C_3H_9N. Reproduced with permission from Elsevier, ref. 61.

the chemical and electronic effects of bimetallic NPs. The adsorbed H_2 molecules were efficiently dissociated into atoms by the Pd–Au NPs, which were then transferred to the SnO_2 surface. There, they reacted with active oxygen ions to form water vapor. Furthermore, the absorption of H_2 by the AuPd alloy NPs and partial formation of PdH_x on SnO_2 decreased the Schottky barrier height. This reduced the thickness of the electron depletion layer, resulting in the generation of a sensing signal.

In another study related to use of AuPd, Pandey *et al.*[59] investigated H_2 detection using AuPd bimetallic NPs. They synthesized SnO_2 nanorods (NRs) using a hydrothermal approach and decorated them with bimetallic AuPd NPs using a reduction method. The optimized sensor showed a high response of 46.4 to 100 ppm H_2 gas at 175 °C. This output was 43-fold higher than that of the SnO_2 sensor and approximately 3 times higher than that of Pd-decorated SnO_2 NRs. This notable sensing characteristic of the optimized gas sensor was attributed to the pronounced catalytic effect of the bimetallic NPs at the sensing temperature and creation of Schottky junctions between the AuPd and SnO_2 NRs.

In a study on the use of AuPd bimetallic NPs, Chen *et al.*[60] prepared ZnO nanowires (NWs) *via* a hydrothermal route under conditions of 140 °C for 12 h. Au, Pd, and AuPd NPs (5–20 nm) were decorated onto these ZnO NWs *via* a chemical route. Fig. 9(a)–(c) show the TEM/HRTEM images of the AuPd NPs on the ZnO NWs. Fig. 9(d) shows the sensing behaviour of gas sensors to 1 ppm NO_2 gas *versus* temperature. The bimetallic AuPd decorated-sensor showed the highest response to 1 ppm NO_2, which was R_g/R_a = 94.2 at 100 °C. This was much higher than that of the Pd-decorated sensor. Furthermore, the response and recovery times were shorter than those of the other gas sensors. Owing to the electronic and chemical sensitization effects of the bimetallic Au/Pd NPs, the Au/Pd-decorated sensor exhibited both higher sensing performance for NO_2 than the Au- and Pd-decorated gas sensors and lower sensing temperature.

Sun *et al.*[61] synthesized monodisperse In_2O_3 porous spheres that were 200–300 nm in size using a hydrothermal approach under the conditions of 130 °C for 12 h. Subsequently, an *in situ* redox process was used to deposit Pd, Au, and bimetallic AuPd NPs onto the In_2O_3 nanospheres. The decorated samples exhibited a higher total number of oxygen vacancies than pristine In_2O_3, with AuPd–In_2O_3 showing the highest percentage. These oxygen vacancies provide additional active sites for both reaction and adsorption. Additionally, higher concentration of adsorbed oxygen species indicates higher involvement of chemisorbed oxygen in the oxidation–reduction processes. At 175 °C, the AuPd–In_2O_3 sensor produced a response of 367 to 100 ppm C_3H_9N and significantly outperformed Pd–In_2O_3 (30.3), Au–In_2O_3 (2.9), and In_2O_3 (1.1) (shown in Fig. 10(a)). The cross-selectivity of the AuPd–In_2O_3 sensor was evaluated by measuring its response to a gas mixture comprising 10 ppm crosstalk gas and 10 ppm C_3H_9N (Fig. 10(b)). The response of the sensor to the gas mixture was nearly identical to its response to C_3H_9N alone, which highlights its ability to differentiate between gases. Furthermore, its high selectivity towards C_3H_9N may be attributed to the low C–N bond energy in C_3H_9N, which enables its ready breakage at the sensing temperature on the sensor surface.

Furthermore, the electron cloud density surrounding the N atom in C_3H_9N is higher than that around the oxygen atoms in other gases, which facilitates the adsorption of the C_3H_9N molecules on the sensing material.

The superior performance of the AuPd bimetal-decorated sensor compared with that of the single noble metal-decorated sensor could be primarily attributed to the synergistic effect of Au and Pd. Both electronic and chemical sensitization enable greater adsorption of oxygen, which significantly increases the resistance of the sensor in air. In addition to the catalytic effects of noble metals, AuPd exhibits hybridization of the s, p, and d orbitals with electron loss in the d-band. This phenomenon in association with the catalytic behavior enhances the effectiveness of the AuPd alloy particles as catalytic sites.

The hierarchically assembled structure provides a high surface area, effective charge-transfer pathways, facile charge flow, and numerous active sites, all of which contribute to enhanced sensing performance. Zen *et al.*[62] synthesized hierarchical WO_3 NW bundles *via* a facile hydrothermal route at 180 °C for 20 h. They were composed of several bundles of well-ordered NWs of

uniform size. The bundles comprised an assembly of multiple 1D NWs that formed hierarchical structures with straight nanowire arrangements. A single NW with a diameter range of 5–10 nm naturally forms uniform bundles approximately 50–100 nm in size. The average diameter of these hierarchical bundles was approximately 500 nm, and the length was 3–4 μm. Additionally, Au NPs with diameters of approximately 4–16 nm were dispersed across the surface of the WO_3 bundles, whereas the size of the AuPd NPs was 5–24 nm. The AuPd–WO_3 sensor was decorated with 2.4 wt% Au and 0.48 wt% Pd and exhibited a significant response of 91 to 50 ppm *n*-butanol at 200 °C, which was approximately 14-fold and 1.4 times higher than those observed for pristine WO_3 (5.7) and Pd–WO_3 (59) sensors, respectively. Alkyl chains containing *n*-butanol cause significant surface adsorption and dissociation. The $-CH_3$ group acts as an electron-donor and enhances the electron density on the oxygen atom. The –OH group possesses higher polarity and lower bond energy than the C = O group in C_3H_6O. Therefore, *n*-butanol exhibits notable electron-donating capability that enables chemisorbed oxygen species to interact with butanol at lower concentrations than those of other gases. Moreover, decorating WO_3 particles with AuPd NPs resulted in synergistic effects, which could be attributed to the spillover effects of oxygen and *n*-butanol. In the AuPd-decorated WO_3, the electrons are transferred from WO_3 to Pd and Au. Then, the EDL expands on WO_3, and band bending occurs; however, upon exposure to *n*-butanol, the height of the barrier reduces, leading to the generation of a sensing signal.

Three-dimensional ordered macroporous (3DOM) structures show advantages such as a large surface area and pores for easy diffusion of gases. Therefore, they are good candidates for sensing applications.[63] Zeng *et al.*[64] synthesized 3DOM WO_3 with a macropore size of 320 nm and decorated it with bimetallic AuPd NPs. Among the different gas sensors, the AuPd-decorated sensor showed the highest response of 28 to 10 ppm C_3H_6O at 300 °C. The sensor successfully detected C_3H_6O in the exhaled breath of individuals with diabetes. The pores in 3DOM WO_3 facilitate the diffusion of gases. Additionally, the oxygen molecules dissociate into oxygen ions *via* the spill over effect of the AuPd alloy, leading to the expansion of the EDL. Hence, an increased degree of resistance modulation occurs in the bimetal-decorated gas sensors. Furthermore, electronic sensitization owing to the formation of Schottky junctions contributes to the enhanced sensing mechanism.

Li *et al.*[65] decorated Pd, Au, and AuPd bimetallic NPs (3–10 nm) on SnO_2 NSs that were fabricated using a solvothermal reaction at 180 °C for 12 h with ascorbic acid as the reducing agent. Compared with that of $NaBH_4$, ascorbic acid shows weaker reducing properties, which results in the formation of fewer seeds. Therefore, the AuPd NPs exhibit good dispersibility and are less prone to aggregation. The AuPd-decorated SnO_2 sensor demonstrated a response of 6.6 to 2 ppm C_3H_6O at 250 °C and 4.1 to 2 ppm HCHO at 110 °C. It showed notable selectivity for the detection of C_3H_6O at low concentrations (Fig. 11(a)) with a minimal or negligible response to other biomarkers (Fig. 11(b)). The presence of interfering gases

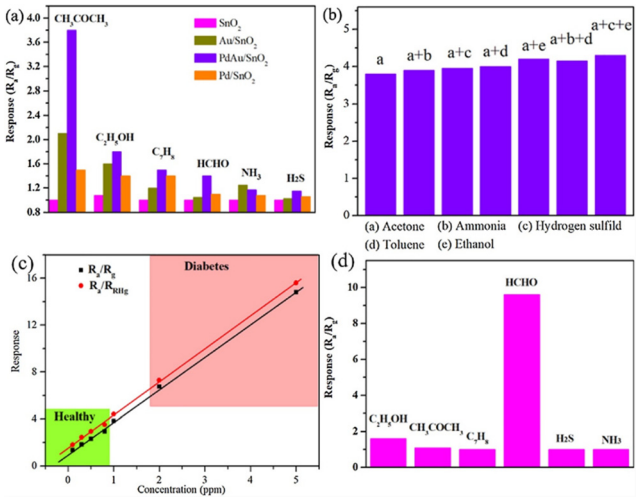

Fig. 11 Sensing tests of the AuPd/SnO_2 sensor: (a) selectivity graph; (b) discrimination test of the response to the mixed gas (1 ppm C_3H_6O and 1 ppm other interference gases); (c) response to different concentrations of C_3H_6O in a 94% RH environment at 250 °C; and (d) AuPd/SnO_2 sensor selectivity at 110 °C. Reproduced with permission from Elsevier, ref. 65.

elicited little effect on the C_3H_6O response of the sensor with a maximum response variation of only 0.4. This confirmed its high selectivity and strong anti-interference performance. Moreover, the conditions of exhaled breath (94% relative humidity (RH)) were replicated to assess the output in detecting C_3H_6O (Fig. 11(c)). The response showed a slight increase while maintaining the same linear relationship as that in ambient air. This confirmed the ability of the sensor to accurately detect low concentrations of C_3H_6O biomarkers under high RH conditions. Additionally, at low temperatures, the AuPd/SnO_2 sensor exhibited outstanding sensing performance (Fig. 11(d)).

Au NPs are recognized as chemical sensitizers owing to their "spill over effects." They act as highly efficient catalysts for oxygen dissociation and outperform SnO_2. Furthermore, they facilitate the catalytic decomposition of molecular oxygen. The activated oxygen species generated during this process are subsequently transferred to the surface of the metal oxides. The high concentration of the chemisorbed oxygen ions increases the thickness of the EDL and raises the baseline resistance in air, which enhances sensitivity. Additionally, oxygen ion adsorption occurs on the surface of the metal nanoparticles at low temperatures and is facilitated by the high conductivity and availability of free electrons in Au. This phenomenon possibly facilitates a rapid and efficient reaction between the detected gas molecules and adsorbed oxygen. Moreover, the electronic sensitization effect of Pd plays a crucial role in enhancing the sensitivity and selectivity toward C_3H_6O and HCHO.

Listeria monocytogenes is a fatal foodborne pathogen that is found in vegetables, fish, and dairy products.[66] *L. monocytogenes* causes severe illnesses even at low levels of infection, particularly in pregnant women, newborns, and the elderly. The mortality rate associated with this pathogen is 20–30%.[67] 3-Hydroxy-2-butanone is a key biomarker for the growth of

L. monocytogenes,[68] and its concentration increases as culture time increases. Xie[69] synthesized flower-like WO_3 using a solvothermal route at 160 °C for 16.5 h and decorated it with different quantities of Au, Pd, and AuPd NPs using a reduction method. The hierarchical WO_3 NPs were approximately 2 μm in diameter and comprised NSs that were approximately 26 nm thick. Among the different gas sensors, the one with 1 wt% AuPd showed the highest response of 400 to 10 ppm 3-hydroxy-2-butanone at 250 °C. Furthermore, an increase in decoration to >1 wt% covered the effective active regions on the surface of the sensing material, which reduced the response. These results categorically show the notable selectivity of the 1 wt% AuPd–WO_3-based sensor. The large specific surface area provides an extensive active area for surface chemical reactions and numerous pathways for gas transport. Furthermore, the catalytic effects of the bimetallic noble metals and formation of Schottky barriers contribute to the improved response. Additionally, the synergistic effect of the bimetallic AuPd NPs lowers the activation energy, which improves the chemical reactions and produces an enhanced response.

Bimetal-decorated gas sensors can also be used for realization of sensitive CH_4 and H_2S gas sensors. Gas-related disasters, particularly CH_4 explosion and H_2S poisoning, are major threats to coal mine safety. CH_4 is a highly flammable gas that exhibits an explosion limit of approximately 5–15.4 vol%.[70] Furthermore, CH_4 is a potent greenhouse gas, and its global warming effect is approximately 30 times higher on a per-molecule basis than that elicited by CO_2.[71] However, the real-time tracking of gases in coal mines remains a significant challenge because of the complex mine environment, which involves numerous interferences such as dust and steam, and the symmetric nature and strong C–H bonds of the CH_4 structure. Moreover, the materials used in sensors are highly prone to H_2S poisoning. Therefore, $W_{18}O_{49}$ NWs were prepared using a solvothermal route, and their surfaces were decorated with Pd, Au, and Pd@Au bimetallic NPs through ultrasonication.[72] For bimetallic NPs, Pd NPs were synthesized initially as seed materials, followed by the coating of the Pd NPs with Au shells to synthesize Pd@Au bimetallic NPs. The $HAuCl_4$ quantities were set to 0.8 mM, 1.3 mM, and 1.8 mM; the corresponding Pd@Au bimetallic NP-decorated $W_{18}O_{49}$ NWs were named NWs/BNPs-1, NWs/BNPs-2, and NWs/BNPs-3, respectively. Fig. 12(a)–(i) show the microscopic analysis of NWs/BNPs-2, and the Au@Pd bimetallic NPs were found to be evenly distributed across the $W_{18}O_{49}$ NWs. Fig. 13(a)–(d) show the sensing features of the different sensors for various gases. Among different sensors, $W_{18}O_{49}$ NWs/BNPs-2 showed an enhanced response of 7.8 to 1000 ppm CH_4 gas at 320 °C and 55.5 to 50 ppm H_2S gas at 100 °C. Therefore, the sensor exhibits good selectivity for H_2S and CH_4 at both low and high temperatures. Additionally, the response of the sensor to mixed gases (CH_4, H_2S, NO, CO, and NH_3) was tested. Both H_2S and CH_4 gases were successfully detected at their respective optimal temperatures with minimal influence from other gases. The dual selectivity of the $W_{18}O_{49}$ NW/BNP-2 sensor could be attributed to the different activation energies required for the catalytic oxidation of H_2S and CH_4. The $W_{18}O_{49}$

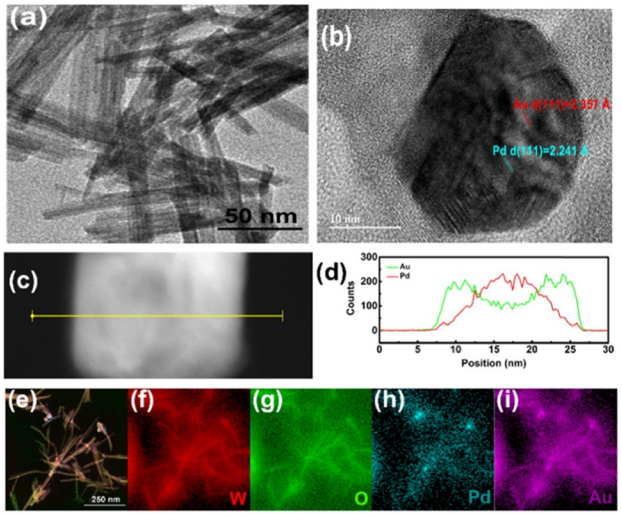

Fig. 12 (a) TEM image of $W_{18}O_{49}$ NWs, (b) HRTEM image of $W_{18}O_{49}$ NWs/BNPs-2 and (c) and (d) EDS elemental line and (e)–(i) surface scans of $W_{18}O_{49}$ NWs/BNPs-2. Reproduced with permission from Elsevier, ref. 72.

NWs provide abundant adsorption sites and efficient transport channels, and oxygen vacancies play a pivotal role in enhancing the gas-sensing performance. At $T \leq 100$ °C, H_2S diffuses deeper into the sensing layer because of its slower rate of reaction, which enables almost the entire sensing layer to participate in H_2S oxidation. However, at high temperatures, the increased catalytic activity of the BNPs causes H_2S to react swiftly with the adsorbed oxygen, which limits its diffusion within the layer and results in a relatively lower response. However, CH_4 requires an elevated temperature for catalytic oxidation because of its stability. At lower temperatures, the high symmetry of the molecular

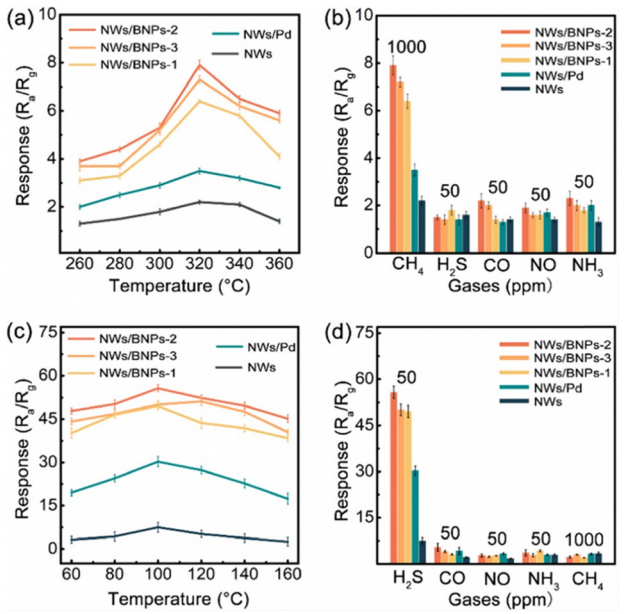

Fig. 13 Response of different sensors to (a) 1000 ppm CH_4 and (c) 50 ppm H_2S *versus* temperature; selectivity of $W_{18}O_{49}$ NWs/BNPs-2 at (b) 320 °C and (d) 100 °C. Reproduced with permission from Elsevier, ref. 72.

structure hinders the oxidation. However, despite CH_4 diffusing deeply into the sensing layer under these conditions, its response remains low. Nevertheless, increasing the operating temperature gradually increases the catalytic activity of BNPs, which increases the number of CH_4 molecules that are oxidized. Subsequently, redox reactions occur at 320 °C, leading to an improved output. Noble metals create Schottky barriers at their interfaces with NWs, which influence the thickness of the EDL and the baseline resistance of the sensor. Additionally, BNPs exhibit varying catalytic activities depending on the temperature, and their catalytic properties enable dual selectivity for distinct gases at varying temperatures.

Overall, AuPd bimetals are among the most promising systems for realization of selective gas sensors towards H_2, CH_4, H_2S, and HCHO gases.

Due to its highly scarce nature, Rh is less studied for gas sensing and in particular bimetallic PdRh NPs are rarely used for gas sensing.[73] In this context, Wang *et al.*[74] synthesized PdRu bimetallic NPs (8 nm) using the polyol synthesis method and used them to decorate (0.1, 0.2, and 0.3 wt%) SnO_2 nanoclusters. The sensor with 0.2 wt% PdRu NPs showed a response of 78.3 to 100 ppm C_3H_9N, which was 14.5 times higher than that of pristine SnO_2 (5.4). At a PdRu loading of >0.2 wt%, the number of adsorbed sites on SnO_2 reduced. This enhanced response may be attributed to the catalytic effects of the PdRu bimetallic NPs toward oxygen and C_3H_9N and formation of Schottky junctions.

In addition to Pd, Pt with similar properties to Pd is widely used in bimetallic systems. In this context, Fan *et al.*[75] synthesized ZnO NRs using a hydrothermal reaction and chemically deposited PtAu, (Pt + Au), Pt, and Au NPs over them. The average sizes of the NPs were 2.92, 2.72, 2.68, and 3.05 nm, respectively (Fig. 14(a)–(h)). Gas-sensing measurements showed that the decorated PtAu alloy NPs showed a high response of 157.4 to 250 ppm H_2 at 130 °C, which was a higher gas response than those of Pt- or Au-decorated sensors (Fig. 15). The boosted response could be attributed to the synergistic effect of the PtAu alloys and formation of a sufficient number of Schottky junctions with the ZnO NWs.

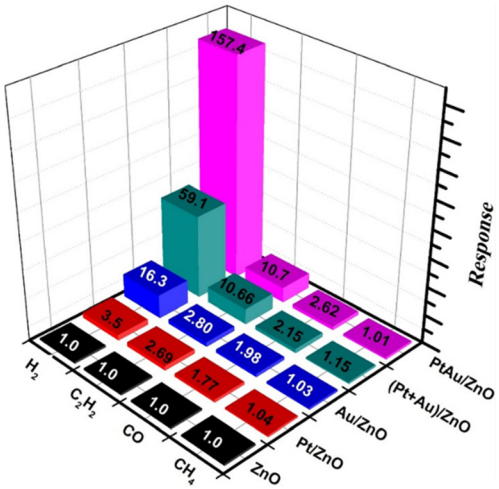

Fig. 15 Selectivity of various gas sensors to 250 ppm gases at 130 °C. Reproduced with permission from Elsevier, ref. 75.

In another work, Liu *et al.*[76] synthesized ZnO NWs using a hydrothermal approach at 140 °C for 12 h and decorated them with Pt, Au, and PtAu NPs *via* a chemical reduction route. The diameter of the ZnO NWs ranged from 90 to 100 nm. They were decorated with approximately 10-nm Au NPs spread uniformly (Fig. 16(a) and (d)) or with significantly small 3-nm diameter Pt NPs clustered densely (Fig. 16(b) and (e)), or with 7-nm diameter PtAu NPs spread evenly (Fig. 16(c) and (f)). At 300 °C, the PtAu-decorated sensor exhibited the highest response (17.7) to 20 ppm H_2S, which was higher than those of the Au-decorated (7.7) and Pt-decorated (7.5) gas sensors. Additionally, the bimetal-decorated sensor exhibited a rapid recovery time,

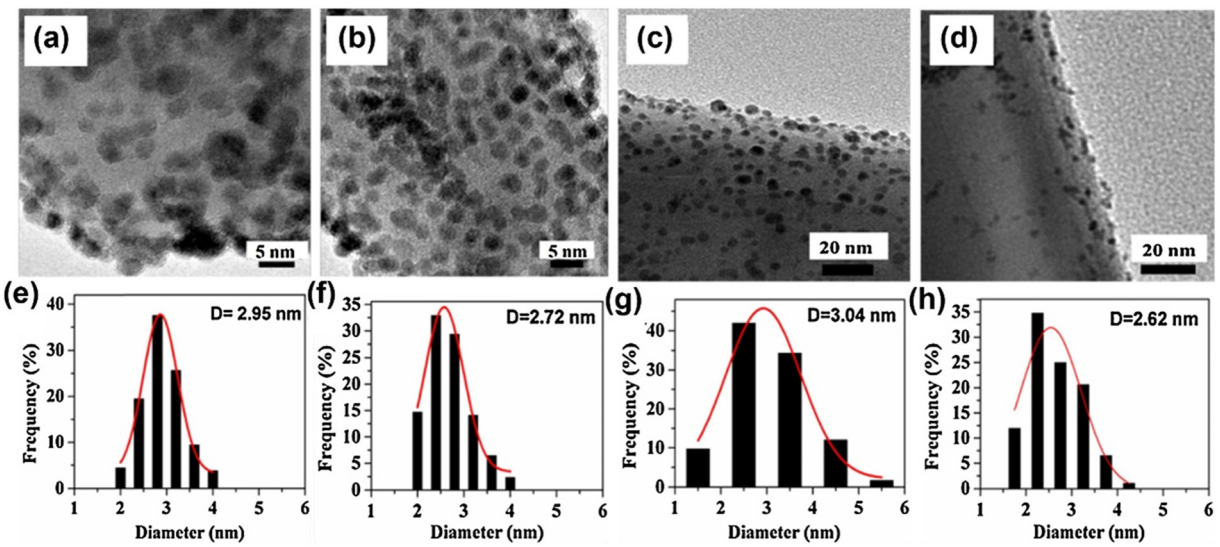

Fig. 14 TEM images and size distributions of noble metal NPs on ZnO: (a) and (e) PtAu/ZnO, (b) and (f) (Pt + Au)/ZnO, (c) and (g) Au/ZnO, and (d) and (h) Pt/ZnO. Reproduced with permission from Elsevier, ref. 75.

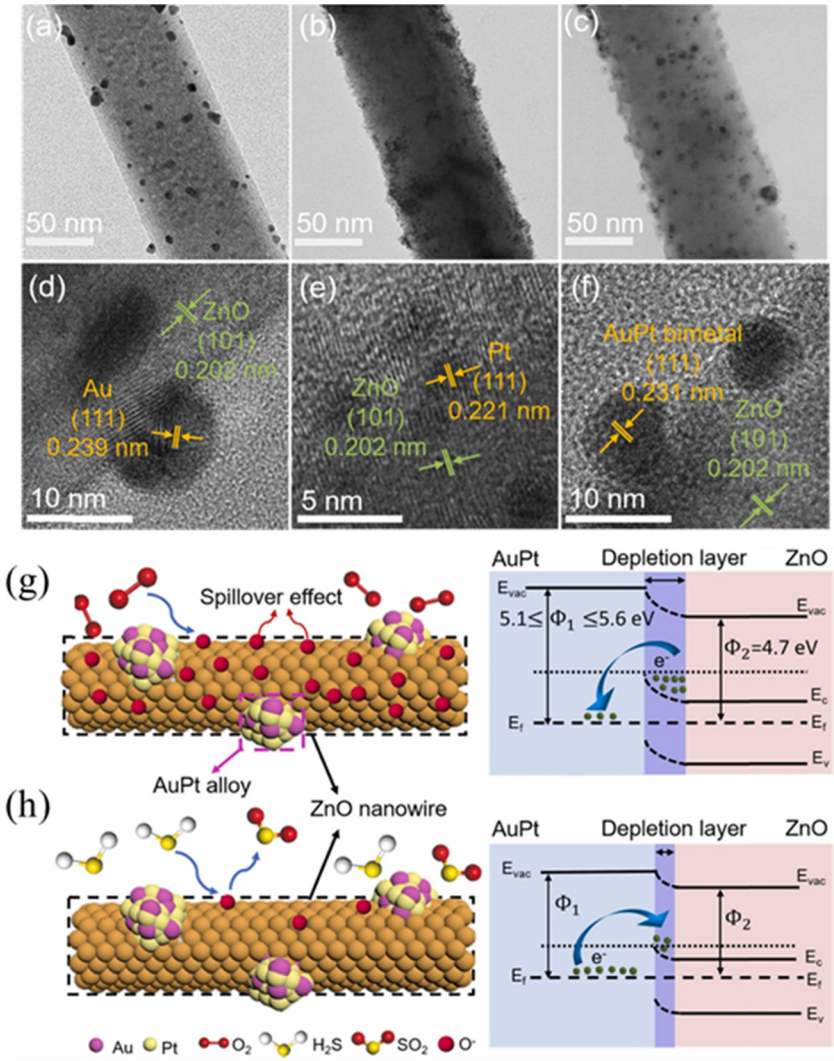

Fig. 16 TEM and HRTEM images of (a) and (d) Au-, (b) and (e) Pt-, and (c) and (f) PtAu-decorated ZnO NWs. The underlying H_2S sensing mechanism of the PtAu-decorated ZnO NWs in (g) air and (h) H_2S gas. Reproduced with permission from Elsevier, ref. 76.

which could be attributed to the synergistic effect between Au and Pt that facilitates the dissociation of adsorbed oxygen. The higher work functions elicited by Au and Pt than that of ZnO enables the formation of Schottky barriers, which increase the resistance in air. Upon the injection of H_2S gas and release of electrons on the sensor surface, the height of the barriers decreases significantly, which produces the sensing signal. Furthermore, the EDL of the ZnO NWs expands in the presence of noble metals, whereas it significantly narrows in the presence H_2S gas, causing an increase in the conductivity of the sensor (Fig. 16(g) and (h)). Furthermore, the distinct spillover and catalytic effects of noble metals boost the sensing output. The PtAu bimetallic NPs effectively catalyse the dissociation of molecular oxygen, which could spill over to ZnO and react with additional H_2S molecules, thereby enhancing the sensing signal.

Also, Peng *et al.*[77] decorated ZnO nanoflowers with Au, Pt, and bimetallic AuPt NPs (1, 3, 6, and 10 wt%) using a hydrothermal method for C_7H_8 detection. The ZnO nanoflowers exhibited diameters of approximately 500–1 μm, whereas those of the Au and Pt NPs were approximately 10 nm. At 175 °C, the sensor with 3 wt% AuPt produced a response of 69.7 to 50 ppm C_7H_8 gas. At a higher AuPt concentration, the NPs occupy the active sites while simultaneously undergoing agglomeration on ZnO. This decreases the performance. The synergistic catalysis of Au and Pt reduces the activation energy required for the C_7H_8-sensing reaction, which accelerates the interaction between the target gas and chemisorbed ions. Furthermore, the Schottky barriers that were formed enable the thickening of the depletion layer, which prevents the recombination of separated electron–hole pairs and facilitates the reaction between more chemisorbed oxygen ions and the target C_7H_8 gas. This results in the release of additional electrons, which alters the resistance and enhances the response of the sensor. The low bond dissociation energy of C_7H_8 plays a crucial role in enhancing selectivity. A low energy requirement for bond dissociation indicates that the chemical bonds are more likely to break, leading to increased sensing reactions.

In another work, Sui *et al.*[78] decorated In_2O_3 NFs with Au, Pt, and bimetallic PtAu NPs. The distinctive 1D architecture provides abundant chemically active sites and facilitates effective electronic transport, making it well-suited for gas-sensing applications. The PtAu NPs exhibited a spherical morphology with a uniform size distribution ranging from approximately 8 to 11 nm. The oxygen ions facilitate the sensing reactions and increase the sensitivity of the sensor. The sample with bimetallic decoration showed higher quantity of adsorbed oxygen ions because of the ''spillover effect'' of Au and Pt. The response of the 1 wt% bimetal-decorated sensor to 110 ppb O_3 was 10.3 at 90 °C. Additionally, it showed a response of 7.1 to 50 ppm C_3H_6O at 240 °C. O_3 and C_3H_6O gas sensing by In_2O_3 NFs was measured at different PtAu NP concentrations (0, 1, and 5 wt%). As the loading concentration increased to 5 wt%, the gas response notably declined. A moderate loading of 1 wt% bimetallic NPs effectively forms Schottky barriers at the interfaces, which enhance electron transfer *via* the spillover effect. In contrast, a loading of >1 wt% showed significant agglomeration of noble metals, which diminished their catalytic activity and consequently reduced the gas response. Exhaled breath samples were collected from 10 healthy participants, of whom five were males and five were females. Then, 1.8 ppm C_3H_6O was added to one of the samples to simulate diabetic breath, as this concentration is considered a significant threshold for diabetes diagnosis. The sensor exhibited a stronger response to diabetic breath than to healthy breath and effectively distinguished the two samples. This demonstrates the potential of PtAu-decorated In_2O_3 NF sensors for the clinical diagnosis of diabetes. Au incorporation modifies the Pt–Pt bond length and alters the heteroatomic coordination number. Consequently, the d-band center shifts and reflects the reduced binding energy of Pt within the heterostructure. This leads to enhanced electrocatalytic activity of PtAu compared with those of Au or Pt. The uniform size distribution and even distribution of the PtAu NPs across the fiber surface without any aggregation provide additional active sites and enhance catalytic efficiency. Thus, the In_2O_3 NFs undergo chemical sensitization through the PtAu NP-mediated spillover effect, which facilitates the decomposition and activation of molecular oxygen. Additionally, Schottky barriers are created at the junction between the In_2O_3 NFs and AuPt NPs, which increases the thickness of the EDL. Thus, varying the EDL thickness in the gas atmosphere produces a pronounced change in the resistance.

Combination of noble metals with transition metals has also been reported for sensing purposes. Deng *et al.*[79] hydrothermally synthesized $WO_3{\cdot}H_2O$ hollow spheres (HSs) and decorated them with bimetallic PtCu NPs using the impregnation route. The maximum response of the 0.02% PtCu/$WO_3{\cdot}H_2O$ HS sensor to 50 ppm C_3H_6O (204.9) was 9.5 times higher than that observed for the original $WO_3{\cdot}H_2O$ HS sensor. A low PtCu quantity produced insufficient catalytic activity, whereas an excessive PtCu quantity caused NP agglomeration. The quantity of adsorbed oxygen in pristine $WO_3{\cdot}H_2O$ HS was 27%, and it increased to 32% after decoration with PtCu. The increased quantity of adsorbed oxygen may be attributed to the spillover effect of oxygen on the PtCu NPs. Moreover, the high quantity of adsorbed oxygen species leads to a higher degree of C_3H_6O oxidation on the bimetal-decorated sensor.

In another work, Gu *et al.*[80] synthesized WO_3 nanoplates using a chemical route and decorated them with $PtNi_3$, Pt_3Ni, and nanoalloys. The resistances of the bimetal-decorated NP gas sensors were higher than those of the pristine sensors. In fact, the variation in the atomic radii of Pt and Ni leads to internal stress that deforms the lattice structure and hinders electron movement, thereby increasing the resistance. Furthermore, the unique electronic structure of transition metals results in a narrow d-band and a high effective electron mass, which restrict electrical conduction primarily to the s-band electrons. Thus, an increase in Ni content significantly enhances the distortion of the lattice and electron scattering (owing to s–d hybridization), resulting in a higher resistance of the bimetal-decorated sensors. Among the different gas sensors, $PtNi_3$–WO_3 exhibited high sensitivity to formic acid and showed a response of 591 to 100 ppm formic acid (FA), which was approximately 30 times higher than that of WO_3. Based on the DFT study, the dispersive force of WO_3 was identified as 35 mJ m^{-2}, which was comparable to its polar force of 38 mJ m^{-2}. This indicates comparable compatibility with both polar and nonpolar gases and accounts for the low gas selectivity of the WO_3 sensor. In contrast, the dispersive force in $PtNi_3$–WO_3 reduced to 19 mJ m^{-2}, whereas the polar force was as high as 39 mJ m^{-2}. This suggests an enhanced sensitivity to polar gases and improved selectivity. Additionally, the order of polarity was determined to be water > formic acid > HCHO > C_7H_8, indicating that $PtNi_3$–WO_3 exhibited higher sensitivity to FA, whereas WO_3 showed higher sensitivity to C_7H_8. Furthermore, unlike that observed for Pt_3Ni, the orbital structure of $PtNi_3$ showed additional hybrid orbitals, such as s–p and s–d hybridization, near the Fermi surface, which could be attributed to Ni doping. Furthermore, a framework that uses machine learning was established for gas prediction and recognition, and FA was identified successfully even in the presence of HCHO and C_7H_8 gases. Additionally, the model exhibited the ability to predict untrained FA concentrations with 90.8% accuracy.

Nair *et al.*[81] prepared carbon nanofibers (CNFs) through electrospinning and decorated their surfaces with bimetallic AuPt NPs (CNFs@Au–Pt) using a chemical reduction method. The optimal Au : Pt weight ratio was determined to be 3 : 1. Furthermore, an increase in the Pt quantity of the bimetallic system induced an irreversible sensing process, which could be attributed to the increased formation of Pt–H bonds on the CNF surface; additionally, this significantly increases the recovery time. The optimal CNF : bimetallic AuPt weight ratio was determined to be 3.5 : 1. At higher ratios, the reduced number of catalytic sites decreases the activity. The sensor exhibited a 48% response to 4 vol% H_2 gas at RT. The incorporation of AuPt bimetallic NPs onto the CNFs suppresses the formation of PdH_x, whereas it increases the number of catalytic sites on the CNF surface for H_2 gas detection. Hence, the sensor exhibited rapid response and recovery characteristics. The H_2 molecules dissociate and adsorb efficiently onto

the Au and Pt surfaces. Thus, incorporating bimetallic AuPt NPs increases the number of adsorption sites and enhances the carrier concentration, which improves conductivity.

In another work related to CNFs, Nair *et al.*[82] reported a flexible gas sensor that used Ni–Pt NPs on CNFs. Compared with those of previously studied sensors,[81] the cost of bimetallic Ni–Pt material and quantity of Pt used in this sensor are much lower. Alloying Ni with Pt or forming bimetallic heterostructures induces variations in the atomic arrangements and electronic structures, which enhances the catalytic activity. The bimetallic ratio of the Ni–Pt NPs was optimized using various molar ratios (1 : 3, 1 : 1, and 3 : 1) on CNFs during synthesis. A higher Ni/Pt ratio (1 : 3) showed high sensitivity to H_2 exposure but initially exhibited an irreversible sensor response. In contrast, a balanced Ni/Pt ratio (1 : 1) showed a reversible sensor response, albeit at reduced sensitivity. A 3 : 1 ratio with increased Ni and reduced Pt proportion in the composition of the Ni–Pt bimetallic system showed enhanced sensitivity and improved sensor recovery. A CNF@Ni–Pt (3 : 1) H_2 sensor was fabricated on flexible polyester films using spin coating, which enabled flexible gas-sensing studies. The sensor response was studied under flat and bent states (Fig. 17(a) and (b)). At the flat state it showed a 13% response to 100 ppm H_2 gas at RT, and no noticeable difference was observed between the responses and currents under either condition (Fig. 17(c) and (d)). Furthermore, no significant resistance drift was observed after bending for up to 120 times (Fig. 17(e)), which confirmed the flexible nature of the gas sensor.

Although Pt-based bimetallic NPs show high potential as catalysts, precise control of their size, shape, composition, dispersibility, and compatibility with support materials (such as oxides or carbon) is crucial for achieving optimal catalytic activity. Therefore, synthesis methods that precisely control the shape and composition of bimetallic NPs are widely sought to optimize their catalytic performance in various applications. Kim *et al.*[83] synthesized bimetallic Pt-based NPs (PtM; M = Pd, Rh, or Ni) using a protein encapsulation method. These NPs were supported on mesoporous electrospun WO_3 NFs. Furthermore, they leveraged the nanoscale cavities of apoferritin proteins to synthesize evenly dispersed PtM NPs with an ultrasmall size of <3 nm. This was possible because of the notably thin protein shell that showed an outer diameter of 12 nm and inner cavity size of 8 nm and accommodated two different metal salts.[25] Additionally, the positively charged protein shell surface inhibited nanoparticle aggregation through electrostatic repulsion. At 300 °C and 90% RH, PtPd–WO_3 NFs showed the maximum response of 97.5 to C_3H_6O at 1 ppm, which was higher than the responses of Pt–WO_3 NFs (24.9 at 1 ppm) and pristine WO_3 NFs (4.3 at 1 ppm). At 350 °C, the PtRh–WO_3 NFs showed a high response of 104 to 1 ppm C_3H_6O, which was much higher than those of the Pt–WO_3 NFs (61 to 1 ppm) and pristine WO_3 NFs (5.7 to 1 ppm). At 300 °C, Pt/NiO–WO_3 NFs exhibited a notable H_2S response of 340 at 1 ppm, which was significantly higher than those of Pt–WO_3 NFs (5 at 1 ppm) and pristine WO_3 NFs (3.77 at 1 ppm). Bimetallic alloyed PtPd or PtRh NPs are expected to be more efficient than Pt NPs in breaking down molecular oxygen and the target substance, which would accelerate the chemical reaction rates in comparison with that of Pt NPs. Furthermore, HRTEM and XPS analyses showed that the oxide phases, such as PtO_x, Rh_2O_3, and PdO, formed during calcination, which further increased the EDL thickness by creating p–n junctions between the n-type WO_3 and p-type oxides. This resulted in higher baseline resistances. Upon exposure to C_3H_6O gas, the EDL thickness rapidly

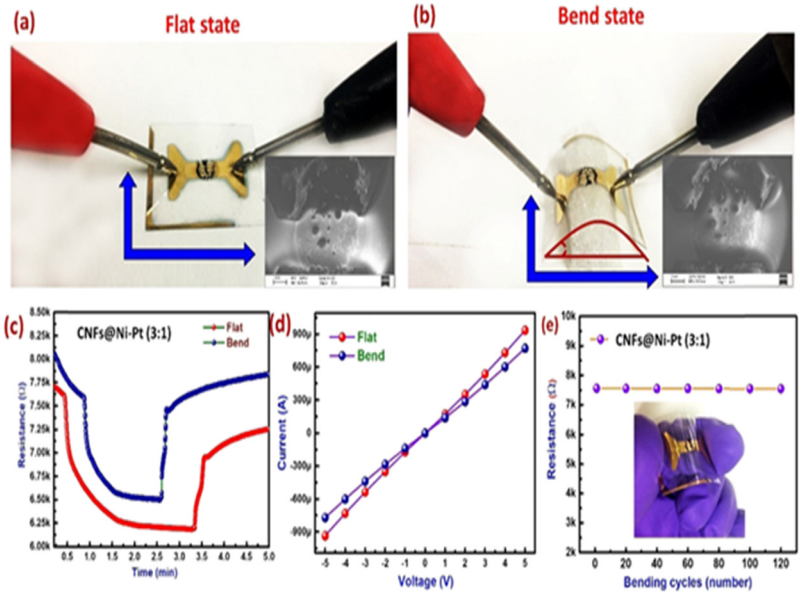

Fig. 17 CNFs@Ni–Pt sensor (3 : 1): (a) flat state and (b) bent state; (c) sensing performance to 1% H_2 at flat and bent states, (d) current–voltage characteristics, and (e) resistance of the flexible CNF@Ni–Pt (3 : 1) sensor *versus* the number of bending cycles. Reproduced with permission from American Chemical Society, ref. 82.

decreases as the electrons returned to the sensor surface. This generates a strong sensing signal. In Pt/NiO–WO_3 NFs, the high reactivity of NiO with H_2S significantly enhances both sensitivity and selectivity toward H_2S. In the Pt/NiO NPs, the Pt phase acts as a chemical sensitizer and facilitates the spillover process, which promotes the dissociation of oxygen and H_2S. The enhanced sensitivity to H_2S may be attributed to the robust interaction between H_2S and the NiO phase. Upon exposure to H_2S, the NiO on the WO_3 NFs was primarily transformed into metallic Ni_3S_2. As the Ni_3S_2 phase is highly conductive, it effectively degrades the p–n junctions, which significantly decreases the resistance of Pt/NiO–WO_3.

PtPd bimetallic NPs are highly favorable for sensing purposes, thanks to their synergistic effect and high catalytic activity. In this context, Li *et al.*[84] prepared In_2O_3 NPs through a hydrothermal method at 130 °C for 12 h and decorated them with Pd and PtPd NPs using a chemical reduction method. In_2O_3 comprised spherical structures formed by NPs of various diameters (100–200 nm). The PdPt-decorated sensor exhibited a high response of 29.8 to 100 ppm H_2 gas, which was >6 times higher than that of the Pd-decorated sensor at RT. The synergistic effect of the bimetallic alloys prevents the oxidation of the Pd catalysts and enhances their catalytic performance. The incorporation of the catalyst significantly increases the concentration of adsorbed oxygen on the sensor, which increases the initial resistance of the sensor and creates additional adsorption sites for subsequent gas reactions. Therefore, once the reaction stabilized, the resistance of the sensor decreased significantly, which produced a pronounced improvement in response. Furthermore, PdPt alloys effectively lowered the activation energy, which facilitated faster oxidation–reduction reactions and higher response levels at low temperatures.

Quantum dots (QDs) are materials with exceptional electrical properties and are widely used in gas sensing applications.[85] In Pd/Pt core–shell QDs, structural and electronic modifications, such as changes in atomic arrangements and chemical potentials at the interfacial areas are expected to enhance H_2 absorption properties. Hassan *et al.*[86] synthesized ZnO NRs using a sol–gel through the hydrothermal route. Then, the Pt/Pd bimetallic QDs were decorated on the ZnO NR clusters using pulsed laser deposition. The Pt/Pd bimetallic core–shell NPs extensively coated the surface of the ZnO NRs and created a uniform and ultrathin film. The core size was approximately 3 nm, whereas the average size of the bimetallic core–shell QDs ranged from 5 to 6 nm. At 50 °C, the bimetal-decorated sensor showed a 70% response to 1% H_2 gas, whereas pristine ZnO NRs showed a response of 65% to the same concentration at 100 °C. This enhanced response could be attributed to the presence of bimetallic QDs on the surface of the sensor. In the case of Pd, H_2 is initially adsorbed onto the surface, followed by dissociation and chemisorption into the Pd lattice to form a Pd hydride (PdH_x). The electrical resistivity of PdH_x is approximately twice that of metallic Pd, which enables H_2 detection through the observed increase in Pd resistance. In contrast, the electrical resistivity of PtH_x was only 21% that of metallic Pt. As shown in Fig. 18(a) and (b) hydride formation did not occur at low temperatures. However, a hydride layer was formed at higher sensing temperatures (Fig. 18(c)), which significantly modulated the resistance of the gas sensor. The Pt/Pd–ZnO NR material exhibited enhanced hydrophobicity owing to the incorporation of the Pd layer, which improved the hydrophobic properties of the surface and acted as a protective barrier. Therefore, the humid environment elicited less effect on the response of the sensor. Moreover, core–shell Au–Pt bimetallic NPs showed enhanced gas response.[87]

Vapor–liquid–solid (VLS) is a feasible method of synthesizing metal oxide NWs with high control over growth parameters, such as temperature, time, and gas flow rate.[88] In this context, Choi *et al.*[89] synthesized SnO_2 NWs *via* VLD. Then, the networked SnO_2 NWs were uniformly decorated with Pd and Pt NPs (10–40 nm) *via* a γ-ray radiolysis process (Fig. 19(a)–(c)). At 300 °C, the pristine sensor showed a response of approximately 40 to 0.1 ppm NO_2 gas; this increased significantly to 880 for the bimetal-decorated sensor (Fig. 19(d) and (e)) along with highly selective behavior toward NO_2 gas (Fig. 19(f)). The enhanced response may be attributed to the synergistic effects of the bimetallic NPs, formation of Schottky barriers, and catalytic effects of the noble metals.

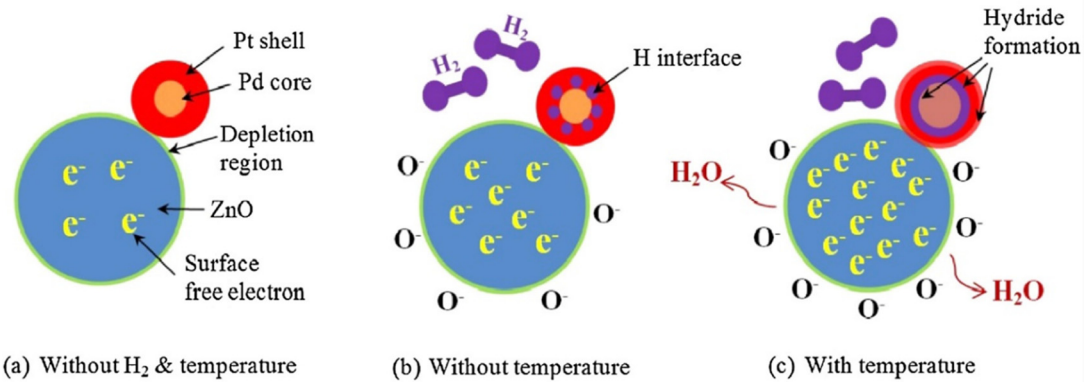

Fig. 18 H_2 sensing mechanism of ZnO NRs decorated with Pt/Pd bimetallic core–shell quantum dots (QDs): (a) in the absence of H_2 at low temperature, (b) in the presence of H_2 at low temperature, and (c) in the presence of both H_2 and elevated temperature. Reproduced with permission from American Chemical Society, ref. 86.

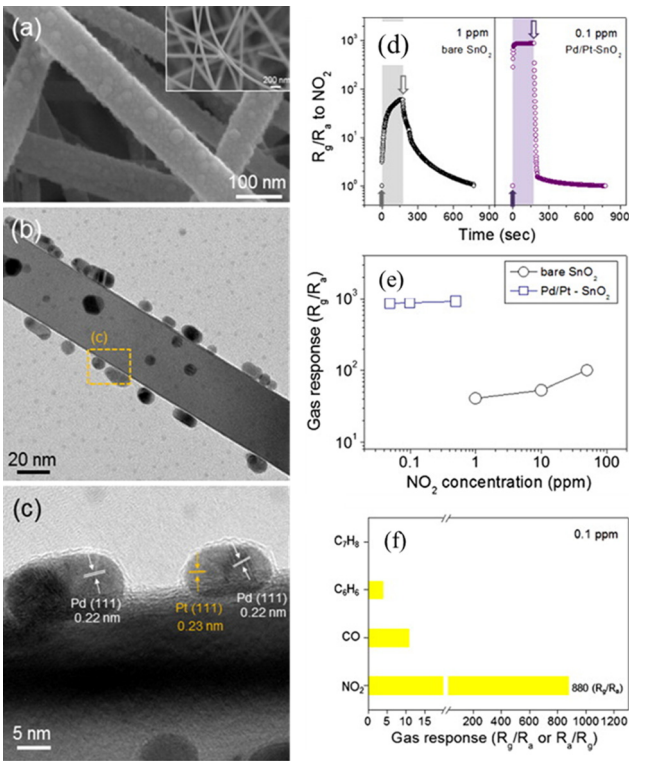

Fig. 19 (a) FE-SEM image of bimetallic Pd/Pt-decorated SnO_2 NWs (inset: pristine SnO_2 NWs). (b) Low- and (c) high-magnification TEM images of bimetallic Pd/Pt-decorated SnO_2 NWs. Response curves of pristine and bimetal-decorated-SnO_2 NW sensors. (d) Response curves of sensors to NO_2 and (e) calibrated response curves for various NO_2 concentrations. (f) Selectivity of the sensor to 0.1 ppm gases. Reproduced with permission from American Chemical Society, ref. 89.

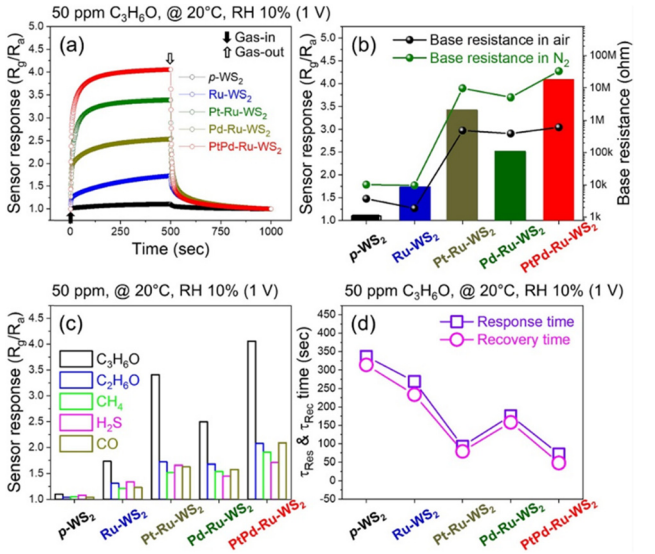

Fig. 20 (a) Sensing plots of various gas sensors to C_3H_6O, (b) corresponding response, and baseline resistance in air and N_2; (c) selectivity curves, and (d) response and recovery times. Reproduced with permission from Elsevier, ref. 92.

Transition metal dichalcogenides (TMDs) have the general formula of MX_2, where M indicates a transition metal and X indicates a chalcogen (S or Se). They exhibit a 2D morphology, high surface area, and high conductivity.[90,91] Therefore, they are good candidates for gas-sensing applications. In a work related to TMDs, Kim *et al.*[92] implanted WS_2 NSs using Ru ions and decorated their surfaces with Pt, Pd, and PtPd bimetallic NPs using UV irradiation. The PtPd-decorated Ru-implanted WS_2 sensor exhibited a response of 4.2 to 50 ppm C_3H_6O at RT, which was higher than those of the other sensors (Fig. 20(a) and (b)). Additionally, it exhibited better selectivity and faster dynamics than those of the other sensors (Fig. 20(c) and (d)). The catalytic effects of the PtPd NPs towards C_3H_6O, generation of sulfur vacancies due to Ru implantation, and generation of Schottky junctions between Pt/Pd and Ru-implanted WS_2 explain the high response of the sensor to C_3H_6O gas.

The shape of the bimetallic NP is an important parameter that affects the sensing response of gas sensors. Meng *et al.*[93] synthesized PdPt nano-octahedra (PdPt NO), PdPt nanocubes (NCs), and PdPt nanoflowers (NFs), as shown in Fig. 21(a)–(f) and decorated them with SnO_2 NPs for gas-sensing studies.

At 50 °C, the PdPt NO–SnO_2 sensor showed a high response of approximately 75 680 to 1000 ppm H_2 gas, which was significantly higher than those of PdPt NCS-, and PdPt NFS-decorated sensors with approximate responses of 19 239 and 907, respectively. To study the effect of the composition of bimetallic NPs on gas response, the performances of the gas sensors at RT were recorded, and the following order was obtained: Pd : Pt = 3 : 1 > Pd : Pt = 4 : 1 > Pd : Pt = 2 : 1 > Pd : Pt = 1 : 1. At a Pd : Pt loading ratio of <3 : 1, the catalytic effect is insufficient to fully expose the surface of the sensitive material to H_2, and only produces a limited improvement in sensitivity. However, at a Pd : Pt loading ratio of >3 : 1, the excessive surface catalytic activity of the sensitive material accelerates the H_2 desorption process, which reduces H_2 adsorption and ultimately lowers the sensor response. Additionally, the sensor exhibited high selectivity towards H_2 gas, which could be attributed to the high catalytic activity of Pd towards H_2 and the small kinetic diameter of H_2 (2.89 Å) compared with that of other gases. Oxygen molecules are primarily adsorbed onto the PdPt NPs, and PdPt catalyses the dissociation of molecular oxygen into atomic oxygen species. Subsequently, the oxygen atoms move to SnO_2 and capture electrons to generate adsorbed oxygen ions. Thus, the PdPt NPs show improved conversion of oxygen molecules into atoms, which accelerates electron flow and enhances the sensing output.

Hollow morphologies are among the most popular morphologies for sensing applications thanks to accessibility of gas molecules to both interior and exterior parts of sensing materials. In this context, Cai *et al.*[94] synthesized the carbon templates using a hydrothermal method d at 190 °C for 9 h. Then, hollow multi-shell SnO_2 nanostructures were prepared using carbon templates. The bimetallic PdPt (2.0 wt%) NPs of sizes 5–10 nm were decorated on them using an *in situ* reduction method. The specific surface area of the multi-shell hollow SnO_2 nanostructures was approximately 65 $m^2\ g^{-1}$, which increased to approximately 110 $m^2\ g^{-1}$ after bimetallic decoration. This may be

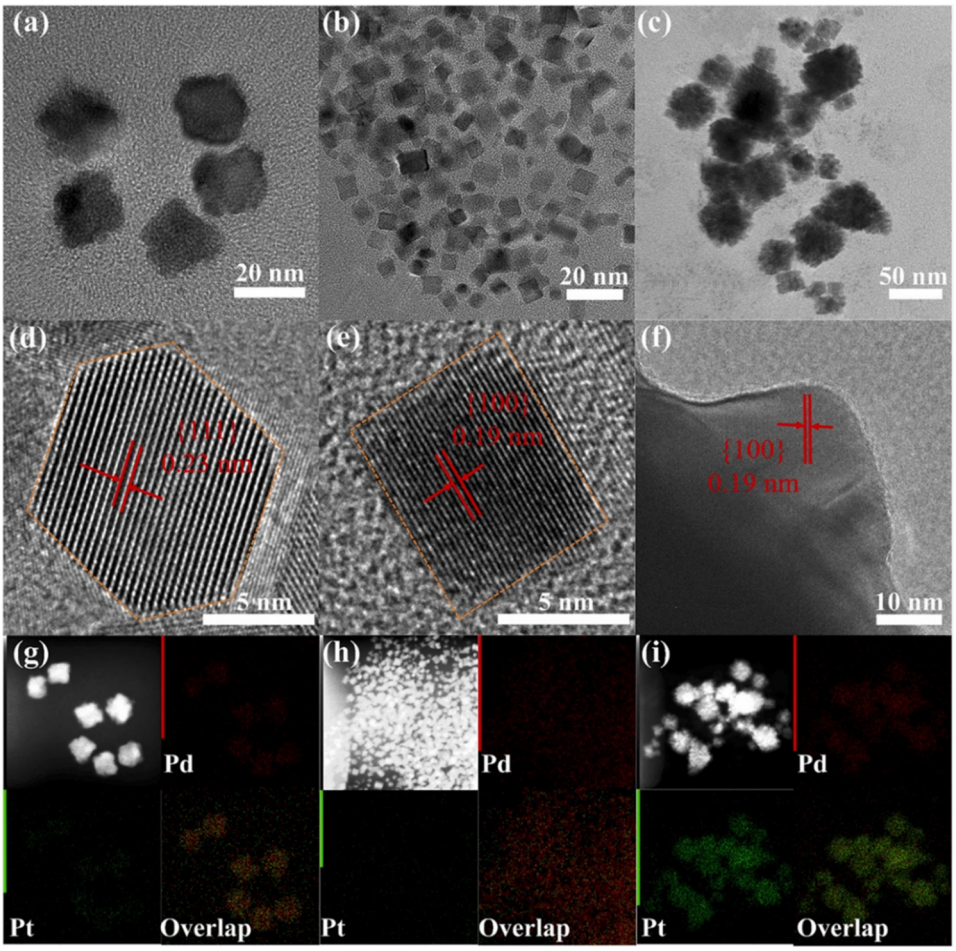

Fig. 21 TEM, HRTEM, and EDS mapping of (a), (d), and (g) PdPt NO, (b), (e), and (h) PdPt NCs, and (c), (f), and (i) PdPt NFs. Reproduced with permission from Elsevier, ref. 93.

primarily attributed to the presence of multiple shells, complex inner construction of the SnO_2 nanostructures, and presence of nanoscale bimetallic NPs. The bimetal-decorated sensor showed a high response of 867% to 1000 ppb HCHO at 190 °C, which was significantly higher than the 32.4% response of the pristine multi-shell sensor. The synergistic effect of PdPt NPs, catalytic activity of the noble metals, and formation of Schottky barriers at the interfaces between the noble metals and SnO_2 account for the enhanced response. Additionally, the response and recovery times of the optimal sensor were 5 and 7 s, respectively. The fast dynamics may be attributed to the distinctive hollow structure and porous shell, which promote the diffusion of HCHO gas. Furthermore, the large specific surface area provides additional reactive sites, which allows the gas molecules to interact with the sensing material and undergo reactions. In contrast, the synergistic effect of bimetallic PdPt decreases the activation energy required for sensing and expedites the reaction between HCHO and the oxygen species, which enhances the rapid dynamic response of the sensor.

Moreover, PtPd bimetallic NPs characterized by a Pd-enriched shell and Pt-enriched core were fabricated and used for decoration of SnO_2 NSs.[95] The optimal bimetallic PdPt content in the PtPd/SnO_2 composite was determined to be 1 wt%. It showed dual selectivity for detecting CO (a response of 6.5 to 1 ppm CO) at 100 °C and CH_4 (a response of 3.1 to 500 ppm CH_4) at 320 °C, which may be attributed to the distinct activation capacities of PdPt NPs for CO and CH_4. Although CH_4 exhibit a significant diffusion depth within the sensing layer at low temperatures, the sensor response was minimal owing to the inherent challenge of CH_4 oxidation under these conditions. The catalytic combustion of CH_4 typically requires high temperatures because of its inherent chemical stability. As temperature increases, the response to CH_4 increases because of the increased catalytic performance of the PdPt NPs. However, at higher temperatures, the CH_4 oxidation reaction is confined to the surface of the sensing layer, which weakens the sensor response. The sensor exhibited good humidity resistance owing to the unique structure of the PdPt bimetal, which comprised a Pd-enriched shell and Pt-enriched core. Pt prevents the formation of PdO on the PdPt surface, which reduces the interaction between water and PdO while maintaining high catalytic activity for CO and CH_4 at high humidity. The enhanced response may be attributed to (i) the chemical sensitization of PdPt NPs, which includes the

activation of target gases and oxygen spillover effect, and (ii) the formation of Schottky barriers at the junction between SnO_2 and PdPt NPs.

Ru is a member of the Pt group and possesses strong catalytic ability. Its oxides have been widely reported to enhance gas-sensing performance.[96] Li *et al.*[97] initially prepared crystalline bimetallic PtRu NPs (3–7.5 nm) using a reduction method (Fig. 22(a)–(g)). Then, they were loaded (0.2, 0.4, and 0.6 wt%) using the impregnation method onto the surface of flower-like WO_3 that was approximately 1–2 μm in diameter and comprised numerous nanosheets that were approximately 24 nm in thickness. The Pt : Ru atomic ratio was determined to be 1.38 : 1 through EDS.

The response of 0.4PtRu–WO_3 sensor to 100 ppm xylene at 170 °C was 261, which was >9 times higher than the response of the 0.4Pt–WO_3 (28) sensor. A higher number of bimetallic NPs on the surface of the sensor results in their agglomeration and a decrease in catalytic activity. Additionally, the optimal sensor exhibited an extremely fast response time of approximately 2 s, which is attributed to the superior catalytic performance of the PtRu NPs. This facilitates the dissociation of a significant number of oxygen molecules, which expedites the surface redox reaction process. The good selectivity of the optimal sensor may be attributed to the presence of a methyl group that acts as the electron donor and increases the electron density on the benzene ring and its reactivity. This facilitates xylene oxidation.

Overall, Pt is one of the best and most widely used noble metals for gas sensing purposes. Combination of Pt with Au, Rh, Ni, and Pd metals can result in development of highly selective gas sensors.

Ag is a noble metal that is less commonly used in bimetallic NPs. In a research work conducted by Hang *et al.*,[98] In_2O_3 nanoflowers decorated with Ag, Au, and Ag_6Au_1 (Ag (6 wt%); Au (1 wt%)) bimetallic NPs were synthesized using a microwave-assisted solvothermal method. Among the various fabricated sensors, the Ag_6Au_1-decorated bimetallic sensor demonstrated a high response of 277 to 5 ppm HCHO at 170 °C, which was 102 times higher than the response of the pristine In_2O_3 sensor (Fig. 23(a)). Additionally, it showed good selectivity to HCHO gas even in the presence of mixed gases. The largest change ratio in response was only 4.1% for Ag_6Au_1/In_2O_3 when HCHO was mixed with CH_3CH_2OH gas. This indicates that interference from gases exerted little effect on the response of the

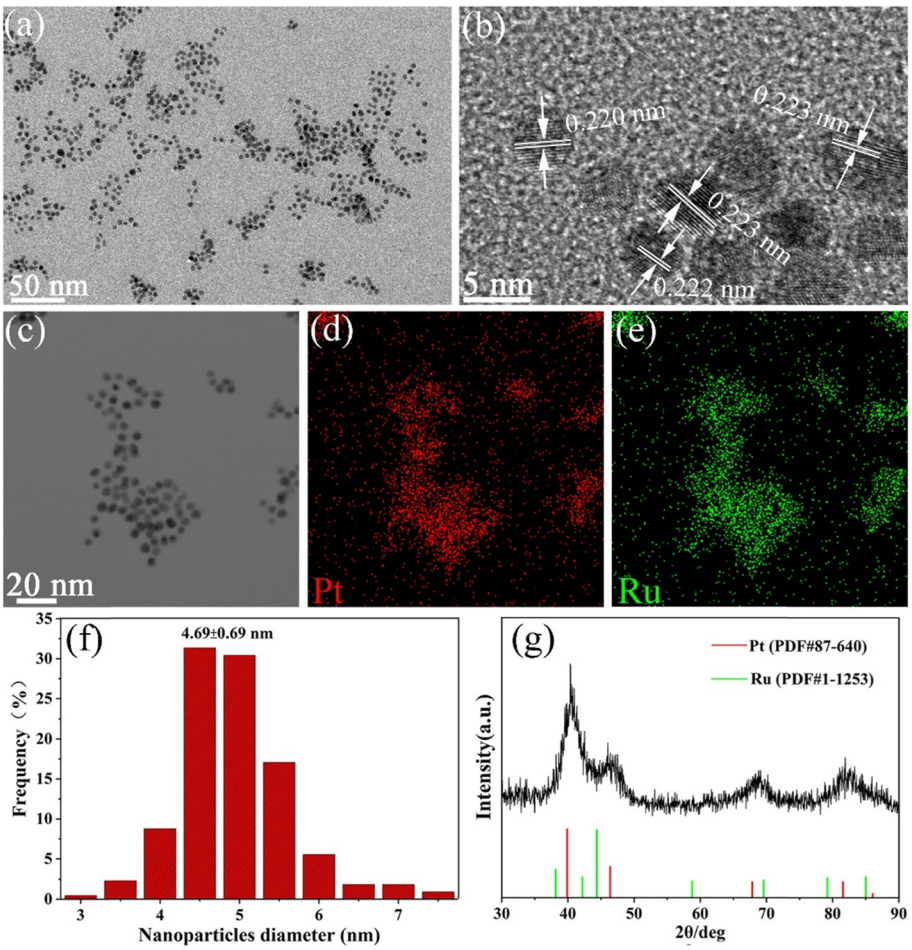

Fig. 22 (a) TEM and (b) HRTEM images of PtRu NCs; (c) STEM image and EDS mapping of (d) Pt and (e) Ru; (f) size distribution of PtRu NCs and (g) XRD pattern. Reproduced with permission from Elsevier, ref. 97.

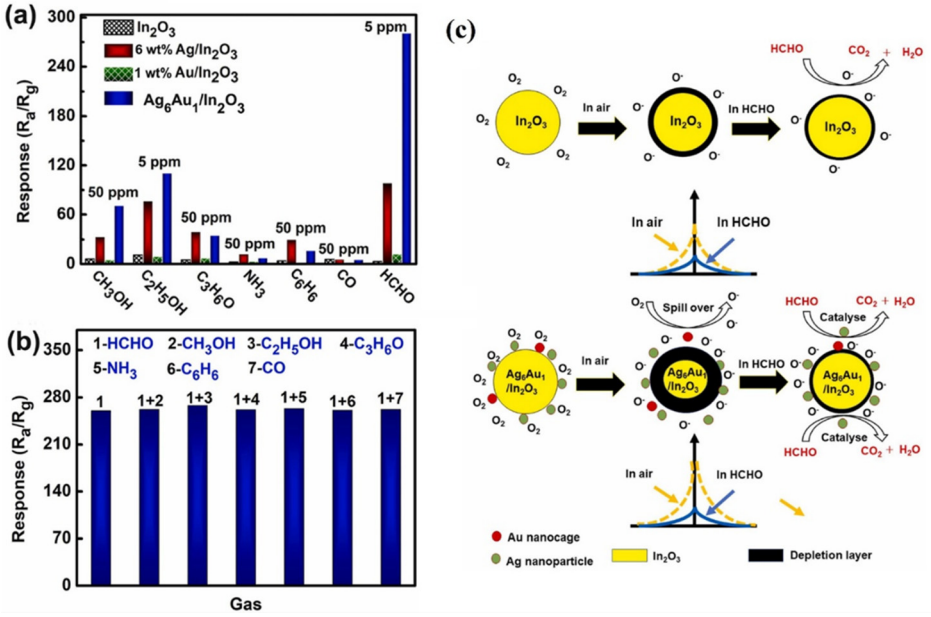

Fig. 23 (a) Selectivity of various gas sensors at 170 °C; (b) discrimination test of the Ag_6Au_1/In_2O_3 sensor to the response of mixed gas with 5 ppm HCHO and 5 ppm other interference gases; (c) HCHO sensing mechanism on the surfaces of In_2O_3 and Ag_6Au_1/In_2O_3 sensors. Reproduced with permission from Elsevier, ref. 98.

Ag_6Au_1/In_2O_3 sensor to HCHO (Fig. 23(b)). DFT calculations showed a notable change in the bond length of HCHO gas in the Ag_6Au_1/In_2O_3 adsorption system, which indicates a strong reaction strength between the HCHO molecules and AgAu/In_2O_3. Moreover, the formation of Schottky heterojunctions and the catalytic effect of bimetallic NPs enhance the response of the optimal sensor. As shown in Fig. 23(c), the EDL thickness significantly changed in the presence of the bimetal-decorated sensor compared with that of the pristine sensor.

Nguyet *et al.*[99] synthesized ultrathin ZnO porous nanoplates *via* a hydrothermal route at 200 °C for 24 h and decorated them with Ag/Pd NPs (approximately 8 nm) by reducing their corresponding salts, followed by ultrasonication. The 0.025 wt% Ag/Pd–ZnO nanoplate sensor showed a high response of 78 to 500 ppm H_2 gas at 400 °C. They found that the catalytic effect of the noble metals was low at low decoration quantity, whereas agglomeration of the noble metals occurred at high decoration quantity. The enhanced performance may be attributed to the catalytic activity of the noble metals and formation of Schottky barriers between the noble metals and ZnO nanoplates. Furthermore, Su *et al.*[100] used Ag to fabricate bimetallic NPs. They decorated the MWCNT/WO_3 nanocomposite with bimetallic Au/Ag NPs (20–85 nm) and investigated its gas-sensing behavior under UV–LED (365 nm) light. The sensor showed enhanced response in an NO_2 atmosphere under UV-LED light. This may be attributed to fact that most of the photogenerated electron–hole pairs swiftly recombine in the absence of the Au–Ag bimetal NPs, whereas the photogenerated electrons transfer to the Au–Ag bimetal NPs in their presence. This prevents the immediate recombination of electrons and holes. Therefore, NO_2 gas molecules directly take the photogenerated electrons and adsorb onto the sensor surface. Hence, the generated sensing signal was higher in the presence of bimetallic NPs and UV light.

3. Conclusion and outlook

We have provided an in-depth explanation of the gas-sensing capacity of bimetal-decorated resistive gas sensors. This review shows that bimetallic decoration is a promising strategy for enhancing the sensing capability in terms of improved sensitivity and selectivity at reduced sensing temperatures. Generally, two noble metals are used for bimetallic decoration, although other metals such as Cu and Ni have been used in combination with noble metals. Thus, various combinations of metals such as AuAg, AuPd, AuPt, PdPt, PtNi, and PtCu have been used successfully to decorate the gas sensors to detect various toxic gases. The most widely used method for decorating metals is the reduction of their salts using a reducing agent. Additionally, the number of bimetallic NPs needs to be optimized to achieve the highest sensing performance. Similarly, the relative quantities of the two metals in bimetallic NPs need to be optimized as they affect the sensing performance. As bimetallic decoration is widely used for metal oxides, more studies related to the bimetallic decoration of 2D semiconductors, such as TMDs and MXenes, are necessary to explore the various effects and aspects of this type of decoration on 2D materials. Furthermore, future studies need to focus on conducting polymers, porous Si, and graphene. Generally, bimetallic decoration significantly enhances the overall sensing performance compared with its pristine and single-metal-decorated counterparts. This is because of the catalytic and electronic effects exerted by the bimetallic NPs.

Future studies in the field of bimetallic decoration can be geared towards exploring the decoration of nanocomposites of metal oxides with other materials, such as MXenes, TMDs, CPs, and graphene. Additionally, future studies are required to determine the effects of amorphous bimetallic materials on sensing performance. Flexible gas sensors that use bimetallic NPs have not been extensively studied; hence, this aspect needs to be investigated further. Similarly, core–shell bimetallic decoration is another aspect that warrants further studies. Finally, this review shows that Rh and Ru noble metals have not been used extensively for decoration.

Data availability

No data were used for the research described in this article.

Conflicts of interest

The authors declare that they have no known competing financial interests or personal relationships that could have appeared to influence the work reported in this paper.

Acknowledgements

This research was supported by the Nano & Material Technology Development program through the National Research Foundation of Korea (NRF) funded by the Ministry of Science and ICT (RS-2024-00412249).

References

1 J. Bollen and C. Brink, *Energy Econ.*, 2014, **46**, 202–215.
2 Y. Jiang, G. Li, S. Wu, F. Duan, S. Liu and Y. Liu, *Ecotoxicol. Environ. Saf.*, 2024, **284**, 117014.
3 P. Makoś-Chełstowska, E. Słupek and J. Gębicki, *Sci. Total Environ.*, 2024, **945**, 173910.
4 Y. Xie, S. Lyu, Y. Zhang and C. Cai, *Materials*, 2022, **15**(21), 7727.
5 A. Mangotra and S. K. Singh, *J. Biotechnol.*, 2024, **382**, 51–69.
6 D. Baskaran, D. Dhamodharan, U. S. Behera and H.-S. Byun, *Environ. Res.*, 2024, **251**, 118472.
7 X. Wu, J. Cui, R. Tong and Q. Li, *Sensors*, 2022, **22**(15), 5608.
8 M. Vakili, P. Koutník and J. Kohout, *Sustainability*, 2024, **16**(4), 1661.
9 J. Mika, P. Forgo, L. Lakatos, A. B. Olah, S. Rapi and Z. Utasi, *Curr. Opin. Environ. Sustainable*, 2018, **30**, 151–159.
10 X. Song, D. Wu, Y. Su, Y. Li, Q. Li and J. Chen, *Sci. Total Environ.*, 2024, **955**, 176839.
11 Y. Chen, G.-H. Dong, S. Li, Y. Liu, S. Li, Y. Guo, C. Wang and G. Chen, *J. Hazard. Mater.*, 2024, **480**, 136433.
12 S. Robertson and M. R. Miller, *Part. Fibre Toxicol.*, 2018, **15**, 1–16.
13 T. Chen, T. Liu, T. Li, H. Zhao and Q. Chen, *Clin. Chim. Acta*, 2021, **515**, 61–72.
14 P. Hajivand, J. C. Jansen, E. Pardo, D. Armentano, T. F. Mastropietro and A. Azadmehr, *Coord. Chem. Rev.*, 2024, **501**, 215558.
15 Q. Li, W. Zeng and Y. Li, *Sens. Actuators, B*, 2022, **359**, 131579.
16 R. Chen, T. Zhang, Y. Guo, J. Wang, J. Wei and Q. Yu, *Chem. Eng. J.*, 2021, **420**, 127588.
17 L. Kong, Z. Yuan, H. Gao and F. Meng, *TrAc, Trends Anal. Chem.*, 2023, **166**, 117199.
18 S. W. Lee, W. Lee, Y. Hong, G. Lee and D. S. Yoon, *Sens. Actuators, B*, 2018, **255**, 1788–1804.
19 F. Vajhadin, M. Mazloum-Ardakani and A. Amini, *Med. Devices Sens.*, 2021, **4**(1), e10161.
20 A. Mirzaei and G. Neri, *Sens. Actuators, B*, 2016, **237**, 749–775.
21 Z. Wang, M. Bu, N. Hu and L. Zhao, *Composites, Part B*, 2023, **248**, 110378.
22 T. Seiyama, A. Kato, K. Fujiishi and M. Nagatani, *Anal. Chem.*, 1962, **34**(11), 1502–1503.
23 K. G. Krishna, S. Parne, N. Pothukanuri, V. Kathirvelu, S. Gandi and D. Joshi, *Sens. Actuators, A*, 2022, **341**, 113578.
24 G. W. Kumarage and E. Comini, *Chemosensors*, 2021, **9**(8), 197.
25 A. Mirzaei, J.-H. Lee, S. M. Majhi, M. Weber, M. Bechelany, H. W. Kim and S. S. Kim, *J. Appl. Phys.*, 2019, **126**(24), 241102.
26 A. Mirzaei, J.-H. Kim, H. W. Kim and S. S. Kim, *Sens. Actuators, B*, 2018, **258**, 270–294.
27 M. D. El-Muraikhi, A. I. Ayesh and A. Mirzaei, *Surf. Interfaces*, 2025, 106003.
28 J. Zhang, X. Liu, G. Neri and N. Pinna, *Adv. Mater.*, 2016, **28**(5), 795–831.
29 S. Yang, G. Lei, H. Xu, Z. Lan, Z. Wang and H. Gu, *Nanomaterials*, 2021, **11**(4), 1026.
30 V. Arulazi and S. Kalainathan, *J. Mater. Sci. Mater. Electron.*, 2024, **35**(5), 347.
31 S. M. Majhi, A. Mirzaei, S. Navale, H. W. Kim and S. S. Kim, *Nanoscale*, 2021, **13**(9), 4728–4757.
32 A. Mirzaei, H. R. Ansari, M. Shahbaz, J.-Y. Kim, H. W. Kim and S. S. Kim, *Chemosensors*, 2022, **10**(7), 289.
33 G. Liu, Y. Wang, J. Li, Y. Liu and M. Salehabadi, *J. Sulfur Chem.*, 2021, **42**(1), 40–50.
34 Z. U. Abideen, J.-H. Kim, J.-H. Lee, J.-Y. Kim, A. Mirzaei, H. W. Kim, S. S. Kim, Z. U. Abideen, J.-H. Kim and J.-H. Lee, *J. Korean Ceram. Soc.*, 2017, **54**(5), 366–379.
35 A. V. Singhal, H. Charaya and I. Lahiri, *Crit. Rev. Solid State Mater. Sci.*, 2017, **42**(6), 499–526.
36 L.-Y. Zhu, L.-X. Ou, L.-W. Mao, X.-Y. Wu, Y.-P. Liu and H.-L. Lu, *Nano-Micro Lett.*, 2023, **15**(1), 89.
37 G. Li, X. Wang, Q. Li and J. Xu, *Appl. Surf. Sci.*, 2024, **670**, 160688.
38 T. Wang, L. Huang, H. Wu, W. Li, Q. Lu, R. Han, X. Liang, F. Liu, F. Liu and B. Wu, *Sens. Actuators, B*, 2024, **402**, 135105.
39 R. Rajeev, R. Datta, A. Varghese, Y. Sudhakar and L. George, *Microchem. J.*, 2021, **163**, 105910.

40 V. Krivetskiy, K. Zamanskiy, A. Beltyukov, A. Asachenko, M. Topchiy, M. Nechaev, A. Garshev, A. Krotova, D. Filatova and K. Maslakov, *Nanomaterials*, 2019, **9**(5), 728.
41 M. Gholinejad, F. Khosravi, M. Afrasi, J. M. Sansano and C. Nájera, *Catal. Sci. Technol.*, 2021, **11**(8), 2652–2702.
42 M. J. Ahemad, T. D. Le, D.-S. Kim and Y.-T. Yu, *Sens. Actuators, B*, 2022, **359**, 131595.
43 Y. J. Kim, S. Lee, S. Choi, T. H. Eom, S. H. Cho, S. Park, S. H. Park, J. Y. Kim, J. Kim and G. B. Nam, *ACS Sens.*, 2024, **9**(10), 5363–5373.
44 E. Lackner, J. Krainer, R. Wimmer-Teubenbacher, F. Sosada, M. Deluca, A. Koeck, E. Laubender, O. Yurchenko, G. Urban, J. Bekacz, K. Rohracher and E. Wachmann, *IEEE*, 2016, 1–3.
45 H. Yang, Z. Du, Y. Yang, Q. Wu, C. Ma, H. Su, X. Wang and D. Zeng, *ACS Sens.*, 2024, **9**(1), 283–291.
46 R.-J. Ma, G.-D. Li, X. Zou, R. Gao, H. Chen and X. Zhao, *Sens. Actuators, B*, 2018, **270**, 247–255.
47 K. Hassan, A. I. Uddin, F. Ullah, Y. S. Kim and G.-S. Chung, *Mater. Lett.*, 2016, **176**, 232–236.
48 P. Kutukov, M. Rumyantseva, V. Krivetskiy, D. Filatova, M. Batuk, J. Hadermann, N. Khmelevsky, A. Aksenenko and A. Gaskov, *Nanomaterials*, 2018, **8**(11), 917.
49 A. Köck, G. C. Mutinati, E. Brunet, S. Steinhauer, O. Yurchenko, E. Laubender, G. Urban, J. Siegert, K. Rohracher and F. Schrank, *Procedia Eng.*, 2014, **87**, 787–790.
50 A. M. Alwan, D. A. Hashim and M. F. Jawad, *Solid-State Electron.*, 2019, **153**, 37–45.
51 A. M. Alwan, M. F. Jawad and D. A. Hashim, *Plasmonics*, 2019, **14**(6), 1565–1575.
52 A. Mirzaei, H. R. Yousefi, F. Falsafi, M. Bonyani, J.-H. Lee, J.-H. Kim, H. W. Kim and S. S. Kim, *Int. J. Hydrogen Energy*, 2019, **44**(36), 20552–20571.
53 K. Hassan, A. I. Uddin and G.-S. Chung, *Sens. Actuators, B*, 2016, **234**, 435–445.
54 E. Lee, J. M. Lee, E. Lee, J.-S. Noh, J. H. Joe, B. Jung and W. Lee, *Thin Solid Films*, 2010, **519**(2), 880–884.
55 J.-Y. Kim, K. Choi, S.-W. Kim, C.-W. Park, S.-I. Kim, A. Mirzaei, J.-H. Lee and D.-Y. Jeong, *Chemosensors*, 2024, **12**(6), 90.
56 S. J. Park, S. M. Lee, J. Lee, S. Choi, G. B. Nam, Y. K. Jo, I. S. Hwang and H. W. Jang, *Small*, 2025, **21**(2), 2405809.
57 M.-H. Seo, K. Kang, J.-Y. Yoo, J. Park, J.-S. Lee, I. Cho, B.-J. Kim, Y. Jeong, J.-Y. Lee and B. Kim, *ACS Nano*, 2020, **14**(12), 16813–16822.
58 D.-S. Kim, M. J. Ahemad, T. D. Le, H.-J. Lee and Y.-T. Yu, *Mater. Sci. Eng., B*, 2024, **299**, 116939.
59 G. Pandey, S. D. Lawaniya, S. Kumar, P. K. Dwivedi and K. Awasthi, *J. Mater. Chem. A*, 2023, **11**(48), 26687–26697.
60 X. Chen, Y. Shen, P. Zhou, X. Zhong, G. Li, C. Han, D. Wei and S. Li, *Sens. Actuators, B*, 2019, **289**, 160–168.
61 Z. Sun, X. Yan, L. Huang, Y. Zhang, Z. Hu, C. Sun, X. Yang, G. Pan and Y. Cheng, *Sens. Actuators, B*, 2023, **381**, 133355.
62 S. Zeb, X. Peng, Y. Shi, J. Su, J. Sun, M. Zhang, G. Sun, Y. Nie, Y. Cui and X. Jiang, *Sens. Actuators, B*, 2021, **334**, 129584.
63 Z. Dai, T. Liang and J.-H. Lee, *Nanoscale Adv.*, 2019, **1**(5), 1626–1639.
64 F. Zheng, L. Zhang, Y.-Y. Li, Q. Liu, Z. Li and H.-C. Yao, *ACS Appl. Nano Mater.*, 2021, **4**(3), 2713–2720.
65 G. Li, Z. Cheng, Q. Xiang, L. Yan, X. Wang and J. Xu, *Sens. Actuators, B*, 2019, **283**, 590–601.
66 M. I. Hossain, M. F. R. Mizan, S. H. Toushik, P. K. Roy, I. K. Jahid, S. H. Park and S.-D. Ha, *Food Control*, 2022, **135**, 108796.
67 L. Radoshevich and P. Cossart, *Nat. Rev. Microbiol.*, 2018, **16**(1), 32–46.
68 C.-X. Zhou, R.-J. Mo, Z.-M. Chen, J. Wang, G.-Z. Shen, Y.-P. Li, Q.-G. Quan, Y. Liu and C.-Y. Li, *ACS Sens.*, 2016, **1**(8), 965–969.
69 S. Xie, C. Zhao, J. Shen, J. Wei, H. Liu, Y. Pan, Y. Zhao and Y. Zhu, *ACS Sens.*, 2023, **8**(2), 728–738.
70 T. Aldhafeeri, M.-K. Tran, R. Vrolyk, M. Pope and M. Fowler, *Inventions*, 2020, **5**(3), 28.
71 T. Hong, J. T. Culp, K.-J. Kim, J. Devkota, C. Sun and P. R. Ohodnicki, *TrAc, Trends Anal. Chem.*, 2020, **125**, 115820.
72 W. Zhang, T. Yuan, X. Wang, Z. Cheng and J. Xu, *Sens. Actuators, B*, 2022, **354**, 131004.
73 N. Luo, Y. Chen, D. Zhang, M. Guo, Z. Xue, X. Wang, Z. Cheng and J. Xu, *ACS Appl. Mater. Interfaces*, 2020, **12**(50), 56203–56215.
74 C. Wang, Y. Wang, Y. Y. Li, J. Bai, Y. Li, F. Liu, X. Liang, P. Sun, J. Ma and G. Lu, *Sens. Actuators, B*, 2022, **371**, 132498.
75 F. Fan, J. Zhang, J. Li, N. Zhang, R. Hong, X. Deng, P. Tang and D. Li, *Sens. Actuators, B*, 2017, **241**, 895–903.
76 Y. Liu, L.-Y. Zhu, P. Feng, C. Dang, M. Li, H.-L. Lu and L. Gao, *Sens. Actuators, B*, 2022, **367**, 132024.
77 H. Peng, Y. Liu, Y. Shen, L. Xu, J. Lu, M. Li, H.-L. Lu and L. Gao, *Molecules*, 2024, **29**(7), 1657.
78 N. Sui, X. Wei, S. Cao, P. Zhang, T. Zhou and T. Zhang, *ACS Sens.*, 2022, **7**(8), 2178–2187.
79 L. Deng, L. Bao, J. Xu, D. Wang and X. Wang, *Chin. Chem. Lett.*, 2020, **31**(8), 2041–2044.
80 Y. Gu, D. Chen, T. Wu, J. Hao, Z. Zhang, Z. Zhu, F. Xue, S. He and Q. Li, *Sens. Actuators, B*, 2023, **386**, 133754.
81 K. G. Nair, V. Ramakrishnan, R. Unnathpadi, K. K. Karuppanan and B. Pullithadathil, *J. Phys. Chem. C*, 2020, **124**(13), 7144–7155.
82 K. G. Nair, R. Vishnuraj and B. Pullithadathil, *ACS Appl. Electron. Mater.*, 2021, **3**(4), 1621–1633.
83 S. J. Kim, S. J. Choi, J. S. Jang, H. J. Cho, W. T. Koo, H. L. Tuller and I. D. Kim, *Adv. Mater.*, 2017, **29**(36), 1700737.
84 J. Li, Z. Yuan, Z. Mu, Z. Yang and F. Meng, *Sens. Actuators, B*, 2024, **405**, 135404.
85 A. Mirzaei, Z. Kordrostami, M. Shahbaz, J.-Y. Kim, H. W. Kim and S. S. Kim, *Sensors*, 2022, **22**(12), 4369.
86 K. Hassan and G.-S. Chung, *Sens. Actuators, B*, 2017, **239**, 824–833.
87 H. Zhao, J. Li, X. She, Y. Chen, M. Wang, Y. Wang, A. Du, C. Tang, C. Zou and Y. Zhou, *ACS Sens.*, 2024, **9**(4), 2183–2193.

88 A. Mirzaei, M. H. Lee, K. K. Pawar, S. P. Bharath, T.-U. Kim, J.-Y. Kim, S. S. Kim and H. W. Kim, *Materials*, 2023, **16**(18), 6233.
89 S.-W. Choi, A. Katoch, G.-J. Sun and S. S. Kim, *Sens. Actuators, B*, 2013, **181**, 446–453.
90 M. Chhowalla, Z. Liu and H. Zhang, *Chem. Soc. Rev.*, 2015, **44**(9), 2584–2586.
91 A. Mirzaei, M. Alizadeh, H. R. Ansari, M. Moayedi, H. Safaeian, M. H. Lee, T.-U. Kim, J.-Y. Kim, H. W. Kim and S. S. Kim, *Nanotechnology*, 2024, **35**, 332002.
92 J.-H. Kim, A. Mirzaei, I. Sakaguchi, S. Hishita, T. Ohsawa, T. T. Suzuki, S. S. Kim and N. Saito, *Appl. Surf. Sci.*, 2023, **641**, 158478.
93 X. Meng, M. Bi and W. Gao, *Sens. Actuators, B*, 2023, **390**, 133976.
94 H. Cai, N. Luo, Q. Hu, Z. Xue, X. Wang and J. Xu, *ACS Sens.*, 2022, **7**(5), 1484–1494.
95 G. Li, X. Wang, L. Yan, Y. Wang, Z. Zhang and J. Xu, *ACS Appl. Mater. Interfaces*, 2019, **11**(29), 26116–26126.
96 Y. Li, Z. Hua, Y. Wu, Y. Zeng, Z. Qiu, X. Tian, M. Wang and E. Li, *Sens. Actuators, B*, 2018, **265**, 249–256.
97 Y. Li, H. Wang, Y. Liu, Y. Li, C. Wang, J. Bai, L. Yang, Y. Wang, F. Liu and X. Liang, *Sens. Actuators, B*, 2022, **351**, 130950.
98 J. Huang, J. Li, Z. Zhang, J. Li, X. Cao, J. Tang, X. Li, Y. Geng, J. Wang and Y. Du, *Sens. Actuators, B*, 2022, **373**, 132664.
99 T. T. Nguyet, D. T. T. Le, N. Van Duy, C. T. Xuan, S. Ingebrandt, X. T. Vu and N. D. Hoa, *RSC Adv.*, 2023, **13**(19), 13017–13029.
100 P.-G. Su and J.-H. Yu, *Sens. Actuators, A*, 2020, **303**, 111718.

